Granular flow of rough particles in the high-Knudsen-number limit

By V. K U M A R A N

Department of Chemical Engineering, Indian Institute of Science,
Bangalore 560 012 India

The granular shear flow of rough inelastic particles driven by flat walls is considered in the high-Knudsen-number limit, where the frequency of particle collisions with the wall is large compared to the frequency of inter-particle collisions. An asymptotic analysis is used in the small parameter $\varepsilon = ndL$ in two dimensions and $\varepsilon = nd^2L$ in three dimensions, where n is the number of particles (per unit area in two dimensions and per unit volume in three dimensions), d is the particle diameter and L is the distance between the flat walls. In the collision model, the post-collisional velocity along the line joining the particle centres is $-e_n$ times the pre-collisional velocity, and the post-collisional velocity perpendicular to the line joining the particle centres is $-e_t$ times the pre-collisional value, where e_n and e_t are the normal and tangential coefficients of restitution. In the absence of binary collisions, a particle which has a random initial velocity tends to a final state where the translational velocities are zero, and the rotational velocity is equal to $(-2V_w/d)$, where V_w is the wall velocity. When the effect of binary collisions is included, it is found that there are two possible final steady states, depending on the values of the tangential and normal coefficients of restitution. For certain parameter values, the final steady state is a stationary state, where the translational velocities of all the particles reduce to zero. For other parameter values, the final steady state is dynamic state where the translational velocity fluctuations are non-zero. In the dynamic state, the mean-square velocity has a power-law scaling with ε in the limit $\varepsilon \to 0$. The exponents predicted by the theory are found to be in quantitative agreement with simulation results in two dimensions.

1. Introduction

Theories for rapid flows of granular material have been developed based upon the kinetic theory approach for dense gases. Such approaches make an analogy between the motion of the particles in a granular material and the motion of molecules in a gas, and attempt to write down constitutive relations similar to those derived by the Chapman–Enskog procedure for hard-sphere gases (Chapman & Cowling 1970). There have been many formulations of the balance laws and constitutive relations for smooth inelastic particles (Savage & Jeffrey 1981; Jenkins & Savage 1983; Lun *et al.* 1984; Jenkins & Richman 1985). In the generalized Navier–Stokes models, the mass and momentum equations are similar to those for a simple fluid, but the energy equation has an additional term due to the dissipation of energy in inelastic collisions (Jenkins & Savage 1983; Lun *et al.* 1984; Sela, Goldhirsch & Noskowicz 1996; Sela & Goldhirsch 1998). In the moment expansion models (Jenkins & Richman 1985),

the higher moments of the velocity distribution function are incorporated into the description. There have been systematic derivations of hydrodynamic equations up to Burnett order, starting from the Boltzmann equation using an expansion with the Knudsen number and the inelasticity of the particle collisions as the small parameters (Sela *et al.* 1996; Sela & Goldhirsch 1998; Brey *et al.* 1998; Kumaran 2004). A recent review (Goldhirsch 2003) concluded that hydrodynamic models have been unusually successful in describing rapid granular flows.

The above theories usually assume that the single-particle velocity distribution is close to a Maxwell–Boltzmann distribution, and deal exclusively with the low-Knudsen-number regime, where the mean free path (or particle diameter) is small compared to the macroscopic scale. Since the momentum and energy conservation equations are second-order partial differential equations in the spatial coordinates, it is necessary to prescribe boundary conditions for the velocity and the temperature at the boundaries. Jenkins & Richman (1986) have, for example, derived momentum and energy flux conditions at the boundaries by averaging over the interactions of a particle with the boundaries. This flux turns out to be sensitive to the nature of the particle interaction with the boundary. The effect of boundaries on the higher moments of the velocity distribution were also incorporated in the analysis of Kumaran (2000) based on a moment expansion technique.

There are practical situations, such as the flow in thin layers, where the distance between boundaries could be of the order of a few particle diameters, and the Knudsen number is not small. It is important to determine whether the continuum description based on the low-Knudsen-number approximation is valid in this regime as well, or whether a very different description is necessary. While the low-Knudsen-number regime has been relatively well characterized, the successful modelling of the finite-Knudsen-number regime requires some asymptotic results for the dependence of the stress on the strain rate of the system in the limit of high-Knudsen-number. Clearly, the rheology can be local only when the macroscopic scale is large compared to the mean free path. In the high-Knudsen-number limit where the macroscopic scale (channel width) is of the same magnitude as the mean free path, the rheology is not local, and a relationship between the local stress and local strain rate cannot be established. However, high-Knudsen-number flows are often encountered in practical applications in granular flows, and so it is of importance to be able to predict the stress required for a given relative wall velocity and channel width. In such cases, it is not possible to obtain a differential equation relating the local stress and strain rate; the best one can do is to obtain a relationship between the macroscopic stress (stress on the walls) and apparent strain rate (velocity difference divided by channel width). A constitutive relation of this type will have viscometric parameters which are dependent on the channel width, in addition to the apparent strain rate and particle properties. The objective of the present analysis is to determine these constitutive relations, and examine their dependence on the channel width and particle properties. It is also of interest to examine whether the 'Bagnold law', which states that the stress is proportional to the square of the strain rate, is applicable to the high-Knudsen-number regime.

The ratio of the Bagnold coefficients in the high- and low-Knudsen-number regimes may be important for determining whether a granular flow is likely to flow homogeneously or to slip at the boundaries. If the Bagnold coefficient in the high-Knudsen-number regime is much lower than that in the low-Knudsen-number regime, it is possible to envisage a situation where the strain rate in the flow is large in a thin mobile layer for which the mean free path is comparable to the thickness of

the layer, while the bulk of the flow has very little deformation. However, it should be noted that the Bagnold coefficient in the high-Knudsen-number limit is likely to be sensitive to the width of the flowing layer as well as the boundary conditions at the bounding surface. This is in contrast to the low-Knudsen-number regime, where the constitutive relation does not depend on the macroscopic scale.

Hydrodynamic equations for the momentum and energy cannot be written in the high-Knudsen-number limit, because the mean free path is not small compared to the macroscopic scale. In this case, it is necessary to use a more fundamental approach, where the Boltzmann equation is solved directly to obtain the distribution function. It should be noted that the Boltzmann equation is non-local, because the collision integral involves discontinuous changes in the particle velocities during collisions, whereas a hydrodynamic description in terms of the mass, momentum and energy is strictly local. Hydrodynamic descriptions usually use the near-equilibrium approximation, where the distribution function is assumed to be close to the Maxwell–Boltzmann distribution. To describe non-equilibrium phenomena, a perturbation expansion in the ratio of the mean free path and the macroscopic scale is used to derive balance equations for the conserved variables, which are the mass, momentum and energy. Such an approach cannot be used in the high-Knudsen-number limit, because the mean free path is not small compared to the macroscopic scale, and the distribution function could be very different from the equilibrium Maxwell–Boltzmann distribution. In this case, it is necessary to first determine an analytical expression for the distribution function in some well-defined limit. This is difficult, in general, because the constitutive relation in the high-Knudsen-number regime is likely to depend on the details of the particle–wall interactions, and it may not be possible to obtain analytical results in all cases.

The high-Knudsen-number limit has been extensively studied in rarefied gas dynamics (Cercignani 1988), mostly in order to obtain matching conditions for the distribution function in a boundary layer near surfaces, to match two solutions on either side of a shock wave or to relate an initial distribution function to the final Maxwell distribution in the long-time limit. In all of these cases, the objective is to supply the boundary or initial conditions for the outer solution in the boundary region (in space or time). For this, it is necessary to incorporate the details of the particle interaction with the boundary, or of the initial (transient) distribution function in time. Another problem of interest at high-Knudsen-number is the free molecular flow across bounded objects. The approach used here is to neglect the inter-molecular collisions in the leading approximation, and the method of characteristics can be employed to determine the distribution function, which remains unchanged along characteristic directions in the flow. In this case, it is of interest to compute the flux of mass, momentum and energy to the particle, and an accurate form of the kernel for the collision between a particle and the surface is essential for obtaining accurate solutions.

The flow in the high-Knudsen-number limit in channels and tubes with cross-section small compared to the mean free path is an old problem dating back to Knudsen (1909), where one of the important objectives is to predict the flux across a tube as a function of the pressure drop when the tube diameter is small compared to the mean free path (Willis 1962, 1965; Loyalka & Hamoodi 1991). More recently, this problem has become relevant in the context of predicting slip at surfaces in micro-electro-mechanical devices, where the channel width may be small compared to the mean free path, and simulation techniques such as direct simulation Monte Carlo (Liou & Fang 2004) and lattice-Boltzmann (Zhang, Qin & Emerson 2005) have been developed

for these applications. In applications restricted to the high-Knudsen-number limit, intermolecular collisions are neglected, and the details of the wall–particle collision become important in determining the transport rate. Collisions with the wall are modelled either by specular boundary conditions, where the energy of a particle is preserved in a collision, or by an absorption boundary condition where the energy of a particle equilibrates with the thermal energy of the surface, so that the average energy of a molecule is invariant in time. This is very different from a granular flow, because there is no intrinsic thermal energy in the system, and the energy of the particles is provided by the driving at the walls. Therefore, a dynamical steady state with non-zero energy fluctuations can be attained only if there is driving at the walls, and the distribution function is sensitive to the boundary conditions at the walls. In addition, as we shall see in the analysis, a dynamical steady state can be achieved only in the presence of binary collisions, so that the distribution function depends on both the particle diameter and the channel width in the high-Knudsen-number limit. This is a reflection of the fact that the high-Knudsen-number limit usually cannot be analysed using regular perturbation techniques, due to the singular nature of the limiting process.

Analytical results were obtained for the velocity distribution function for smooth particles by Kumaran (1997) using an asymptotic analysis in the small parameter $\varepsilon = ndL$, which is proportional to the inverse of the Knudsen number, where n is the number density, d is the diameter of the particles and L is the channel width. That study was restricted to smooth particles where the angular momentum of the particles was not incorporated into the description, though the particle–wall collision rule did permit the transport of momentum from the wall to the particle in the tangential direction. One of the important findings of this study was that the velocity distribution is highly non-Gaussian and anisotropic. In particular, the mean square of the cross-stream velocity fluctuations is $O(\varepsilon)$ times the mean square of the streamwise velocity fluctuations. In addition, the 'Reynolds stress', which is the average of the product of the streamwise and cross-stream velocity fluctuations, is $O(\varepsilon \log(\varepsilon))$ times the mean square of the streamwise velocity fluctuations. Therefore, the normal stress in the cross-stream direction is small compared to the normal stress in the streamwise direction, while the shear stress is larger than the normal stress in the cross-stream direction. This is in contrast to the flow of nearly elastic particles $(1-e) \ll 1$ in the low-Knudsen-number regime, where the shear stress is $(1-e)^{1/2}$ smaller than the normal stresses. Here, e is the coefficient of restitution. This indicates that there is a significant difference in the nature of the stress between the high- and low-Knudsen-number regimes, and kinetic theories based on the homogeneous shear flow approximation may provide erroneous results in the high-Knudsen-number regime. The predictions of Kumaran (1997) were found to be in agreement with the simulations of Bose & Kumaran (2004).

A similar calculation (Kumaran 1998) was carried out for a vibrated granular material, in the limit where the frequency of collisions with the vibrated surface is large compared to the frequency of inter-particle collisions. The velocity distribution function at steady state was determined by a balance between the flux in and out of a differential interval in the velocity coordinate due to collisions. It was found that the velocity distribution function is sensitive to the nature of the driving by the vibrated surface at the base (symmetric or asymmetric waveform), as well as the nature of the dissipation (inelastic collisions at the base or viscous drag). The distribution functions were shown to be in quantitative agreement with simulations (Kumaran 1999). The leading correction to the distribution function due to binary

collisions between particles was also calculated, and it was found that the distribution function has a power-law dependence on the horizontal velocity in the limit where the velocity goes to zero.

The above studies indicate that the velocity distribution function in the high-Knudsen-number regime is very different from that in the low-Knudsen-number limit even when the coefficient of restitution is close to 1, and the relative magnitudes of the shear and normal stresses for shear flows scale as a power of the parameter ε which is the inverse of the Knudsen number. The disadvantage of the analytical result of Kumaran (1997) was that it is only valid for a specific model of the interaction between the particle and the wall. The particles were assumed to be smooth, and the particle–wall interaction was similar to the type-A boundary conditions of Campbell & Brennen (1985), whereby the difference in the tangential velocity between the particle and the wall is reduced by a constant factor in a collision. This acts as the source of momentum for the particles in the direction tangential to the wall. It is of interest to examine a more detailed particle–wall interaction model, which incorporates the angular velocity of the particles as well as the normal and tangential transfer of momentum at the point of contact for particle–wall and particle–particle collisions. In the present study of rough particles in the high-Knudsen-number limit, a similar procedure is followed to obtain the dependence of the steady-state velocity distribution on a small parameter ε, defined as ndL in two dimensions and nd^2L in three dimensions, where n is the number density of particles (per unit area in two dimensions and per unit volume in three dimensions), d is the diameter of the particle and L is the distance between the walls.

The collision model used here is a modification of the perfectly rough, elastic hard-sphere model which was first formulated by Bryan (Chapman & Cowling 1970). Pidduck (1992) extended the methods developed by Chapman & Enskog, for non-rotating spherical molecules, to rotating hard spherical molecules and obtained expressions for thermal conductivity and viscosity. The constitutive relations for the flow of rough inelastic particles in the low-Knudsen-number regime were considered by Lun (1991, 1996). We use the same model for the high-Knudsen-number regime in the present analysis. A brief description of the model and the simulation technique used for verifying the theoretical results is provided in the §2.1. The steady state in the absence of inter-particle collisions is obtained in §2.2 for a two-dimensional system of sheared disks, while the effect of inter-particle collisions on this steady state is analysed in §2.3. The analysis in §2.3 reveals that there are two possible steady states depending on the normal and tangential coefficients of restitution. In the static steady state, the translational energy of the particles reduces to zero, while in the dynamical steady state, the translational energy of the particles approaches a non-zero value in the long time limit. The distribution function, and the scaling of the moments of the velocity distribution with the parameter ε, in the dynamical steady state are derived in §2.4 for a two-dimensional shear flow of disks. The extension of the analysis to a three-dimensional shear flow of spheres is briefly summarized in §2.5.

2. Theoretical analysis

2.1. *Collision model and simulation technique*

The system consists of a two-dimensional channel of width L containing disks of diameter d, and number density (number of particles per unit area) n. The channel is bounded by two parallel rough walls moving with equal and opposite velocities $+V_w$ and $-V_w$ positioned at $y = +L/2$ and $y = -L/2$, and is considered to be infinite
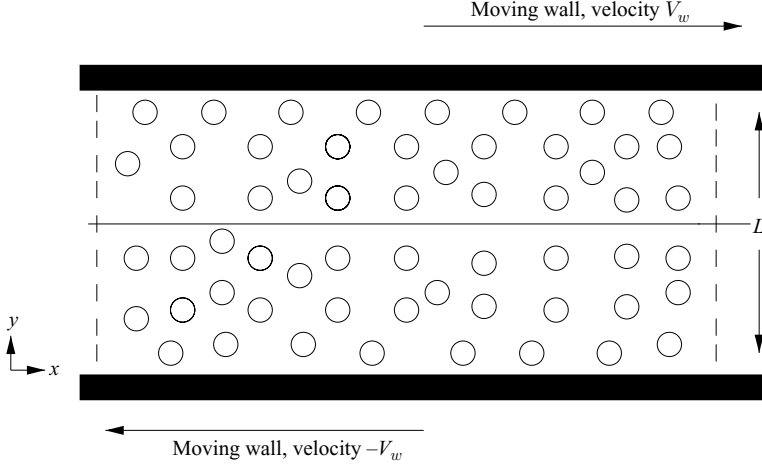
FIGURE 1. Schematic of two-dimensional rough disks sheared with two parallel
moving rough walls.

in the x-direction, as shown in figure 1. For this system, the frequency of particle
collisions with the wall per unit length of the channel is proportional to nu while that
of a particle–particle collision is $n^2 duL$ per length of the channel, where u is the
root-mean-square fluctuating velocity. If the velocity fluctuations are isotropic, the
ratio of the frequencies of particle–particle and particle–wall collisions is given by
the parameter $\varepsilon = ndL$, which is considered to be small in the high-Knudsen-number
limit.

The collision rules for rough, inelastic hard particles, of Lun (1991, 1996), which is
a generalization of the rough elastic particle model of Bryan (1894) (see Chapman &
Cowling 1970), is used here. Two particles, with pre-collisional velocities u_i and u_i^* are
considered, where indicial notation is used to represent the components of vectors.
The post-collisional velocities, u_i' and $u_i^{*'}$ are related by

$$u_i' = u_i + \frac{J_i}{m} \tag{2.1}$$

$$u_i^{*'} = u_i^* - \frac{J_i}{m^*} \tag{2.2}$$

where J_i is the impulse exerted by particle with velocity u_i on particle with velocity
u_i^*. The angular velocities before and after collision are related by

$$d\omega_i' = d\omega_i + \frac{2}{\kappa m}\epsilon_{ijk}k_j J_k \tag{2.3}$$

$$d\omega_i^{*'} = d\omega_i^* + \frac{2}{\kappa m}\epsilon_{ijk}k_j J_k \tag{2.4}$$

where ω_i and ω_i' are particle angular velocities before and after collision respectively,
d is the diameter of the particle, $\kappa = (4I/md^2)$ (m is the mass of the particle and I
is the moment of inertia), and k is the unit vector along the line joining the centre
of the particles directed from the centre of the unstarred particle to the starred
particle. For rough inelastic particles, the impulse exerted is modelled by introducing
the tangential and normal coefficients of restitution, e_n and e_t. In this case, the post-
collisional relative velocity along k is equal to $-e_n$ times the relative pre-collisional
velocity along k, while the relative post-collisional velocity in the plane perpendicular

to k at the point of contact is equal to $-e_t$ times the relative pre-collisional velocity in the plane perpendicular to k. The impulse between the two particles is given by,

$$\frac{J_i}{2m_r} = -\eta_2(u_i - u_i^*) - (\eta_1 - \eta_2)(u_j - u_j^*)k_jk_i + \tfrac{1}{2}\eta_2\epsilon_{ijk}k_j(d\omega_k + d^*\omega_k^*) \qquad (2.5)$$

where m_r is the reduced mass given by $(mm^*)/(m + m^*)$,

$$\eta_2 = \frac{(1 + e_t)}{2}\frac{\kappa}{1 + \kappa}, \quad \eta_1 = \frac{1 + e_n}{2},$$

and e_n and e_t are the normal and tangential restitution coefficients. The limit of smooth elastic particles corresponds to $e_n = 1$ and $e_t = -1$, while the limit of rough inelastic particles (where the tangential velocity at the point of contact is reversed in a collision) corresponds to $e_n = 1$ and $e_t = 1$. For a wall-particle collision, the mass of the wall is considered to be infinite, so that the reduced mass is equal to the mass of the particle, and the angular velocity is assumed to be equal to zero. In this case, the expression for the impulse is

$$\frac{J_i}{m} = -2\eta_2(u_i - u_i^*) - 2(\eta_1 - \eta_2)(u_j - u_j^*)k_jk_i + \eta_2\epsilon_{ijk}k_jd\omega_k \qquad (2.6)$$

where u_i^* is the wall velocity.

Two-dimensional simulations of the flow of rough inelastic disks in a channel were carried out to verify the theoretical predictions. Periodic boundary conditions are applied in the flow (x) direction at the planes $x = \pm L/2$. The event-driven simulations consist of two steps: a streaming step and a collisional step. In the streaming step, the time required for the next impending collision is calculated using the current positions and velocities of all the particles. In the collision step, the velocity of the colliding particles is updated according to equations (2.1) to (2.4). The number of particles in the simulation cell was fixed at 125, and the length and width of the simulation cell were set equal to 1. The diameter of the particles was varied in order to vary the dimensionless parameter $\varepsilon = ndL$ in the range 0.1 to 10^{-4}. The theory developed in §2.4 predicts that the velocity distribution function in the limit $\varepsilon \to 0$ depends only on ε, and not individually on d and n, and it was verified that the results for the velocity moments do not change by more than 1% when the number of particles was increased from 125 to 250 at $\varepsilon = 10^{-4}$ for the coefficients of restitution used here. The number of collisions for the simulations was fixed as follows. As discussed in the introduction, the frequency of particle–wall collisions is large compared to the frequency of particle–particle collisions in the high-Knudsen-number limit. The dependence of the ratio of the frequency of particle–wall to particle–particle collisions, i_m, is derived a little later in equation (2.19). This increases proportionally to $\log(\varepsilon)$ in the limit $\varepsilon \to 0$. In order to obtain accurate averages, it is necessary to vary the total number of collisions with ε in such a way that a particle experiences a large number of binary collisions during the course of the simulation. In the simulations, the system was allowed to equilibrate for $1000i_m$ collisions per particle, and the averages were taken for an additional $1000i_m$ collisions per particle. This ensured that a particle experienced, on average, at least 1000 binary collisions, and a significantly larger number of wall collisions, over the time period of the simulation. The collision ratio i_m is typically in the range 3–20 for the values of ε and the coefficients of restitution studied here, so the total number of collisions in a typical simulation run was of the order of 10^6.

When simulating high-Knudsen-number granular flows, it is necessary to pay attention to two issues. The first is that a large number of periodic images are required in the direction parallel to the plates, in order to capture all collisions, especially those of particles which travel almost parallel to the plates, and travel long distances before colliding with a wall or another particle. This issue was resolved by treating the particle crossing one of the periodic boundaries as an event, and the particle positions were updated for each crossing of one of the periodic boundaries. However, this event was not counted as a collision for the purpose of determining the total number of collisions in the simulation run. This has the advantage that it was not necessary to predict collisions of a particle in the central collision cell with its periodic images, but it has the disadvantage that the times required for the simulation are greatly increased. This is due to the large number of crossings of the periodic boundaries by particles having velocity nearly parallel to the walls between successive particle–particle or particle–wall collisions. The other important issue is that the results of time averaging for the distribution function are not identical to the results obtained by averaging over collisions. This is because the time period between wall collisions is small compared to that between binary collisions, and averaging over collisions results in a bias towards wall collisions. Therefore, in order to determine the distribution function and velocity moments, it is necessary to carry out time averages while calculating the distribution function and the velocity moments.

2.2. Steady state in the absence of inter-particle collisions

In the absence of binary collisions, a steady state is achieved if the particle velocity distribution is recovered after two wall collisions. In the present case, we show by analysing the evolution of a particle velocity due to wall collisions, that the steady-state distribution is a delta function at the location in velocity space where the translational velocities are equal to zero, and the rotational velocity is equal to the ratio of the wall velocity and the particle radius.

If the particle collides with the wall at $y = -L/2$, the particle velocity after a collision obtained from equations (2.1), (2.3) and (2.5), is

$$u'_x = (1 - 2\eta_2)u_x - 2\eta_2\left(V_w + \tfrac{1}{2}d\omega\right), \tag{2.7}$$

$$u'_y = (1 - 2\eta_1)u_y, \tag{2.8}$$

$$\omega' = \omega - \frac{4\eta_2}{\kappa d}u_x - \frac{4\eta_2}{\kappa d}\left(V_w + \tfrac{1}{2}d\omega\right), \tag{2.9}$$

where subscripts x, y stands for flow and gradient directions respectively. The velocity after a subsequent collision with the wall at $y = L/2$ is given by

$$u''_x = (1 - 2\eta_2)u'_x + 2\eta_2\left(V_w + \tfrac{1}{2}d\omega'\right), \tag{2.10}$$

$$u''_y = (1 - 2\eta_2)u'_y, \tag{2.11}$$

$$\omega'' = \omega' + \frac{4\eta_2}{\kappa d}u'_x - \frac{4\eta_2}{\kappa d}\left(V_w + \tfrac{1}{2}d\omega'\right). \tag{2.12}$$

It is convenient to define $\Omega = (\omega + 2V_w/d)$, which is the departure of the angular velocity from its limiting value at long time. With this substitution, equations (2.7) and (2.9) can be written in matrix form,

$$\begin{pmatrix} u'_x \\ \Omega' \end{pmatrix} = \begin{pmatrix} 1 - 2\eta_2 & -\eta_2 d \\ -4\eta_2/d\kappa & 1 - 2\eta_2/\kappa \end{pmatrix} \begin{pmatrix} u_x \\ \Omega \end{pmatrix}. \tag{2.13}$$

Equations (2.10) and (2.12) can be written in the matrix form as

$$\begin{pmatrix} u_x'' \\ \Omega'' \end{pmatrix} = \begin{pmatrix} 1 - 2\eta_2 & \eta_2 d \\ 4\eta_2/d\kappa & 1 - 2\eta_2/\kappa \end{pmatrix} \begin{pmatrix} u_x' \\ \Omega' \end{pmatrix}. \tag{2.14}$$

Considering two successive wall collisions as one event, equations (2.13) and (2.14) can be combined to obtain the velocity of a particle after $(i+1)$ pairs of wall collisions as a function of the velocity after i pairs of wall collisions,

$$\begin{pmatrix} u_x^{(i+1)} \\ \Omega^{(i+1)} \end{pmatrix} = \mathbf{M} \begin{pmatrix} u_x^{(i)} \\ \Omega^{(i)} \end{pmatrix} \tag{2.15}$$

The magnitudes of the eigenvalues of $\mathbf{M}$ provide the rate of decrease in the velocity due to a pair of collisions with the top and bottom walls. We restrict attention, in the reminder of the analysis, to disks of uniform density, for which $\kappa = (1/2)$. However, the scaling relations obtained here are more general, and apply to disks of any density distribution. For uniform disks with $\kappa = (1/2)$, it can easily be verified that the eigenvalues are complex conjugates for $e_t > 0.0294373$, and the magnitudes of the two eigenvalues are equal, $|\lambda_1| = |\lambda_2| = \lambda_{x\Omega}$ (which provides a measure of the amplification or reduction in the magnitude of the eigenvectors in $u_x - \Omega$ space) is equal to e_t. For $e_t < 0.0294373$, the eigenvalues are real and positive, and $\lambda_{x\Omega}$, the rate at which the velocity decreases with the number of collisions, is the larger of the two eigenvalues. In all cases, the magnitudes of the eigenvalues are less than 1, indicating that the magnitude of the two eigenvectors, which are linear combinations of $u_x^{(i)}$ and $\Omega^{(i)}$, decreases monotonically with i. Therefore, in the limit of large i and in the absence of binary collisions, the particle velocities approach $u_x = 0$ and $\Omega = 0$.

The post-collisional velocity of particle in the cross-stream direction after two successive collisions with the wall is obtained from equation (2.8):

$$u_y^{(i+1)} = \lambda_y u_y^{(i)} \tag{2.16}$$

where $\lambda_y = e_n^2$. Since λ_y is also less than 1, the cross-stream velocity of a particle also approaches zero in the long time limit. The above results indicate that one possible steady-state distribution is a delta function at the point in velocity space where the translational velocities are zero, and the rotational velocity is $-V_w/\frac{1}{2}d$.

2.3. *Effect of inter-particle collisions*

First, we provide a qualitative description of the expected final steady states in the presence of binary collisions, and then proceed to quantify them and compare them with simulations. In the presence of binary collisions, there are two possible final steady states. One is the state where all particle velocities decrease to zero at long times, because the frequency of wall-particle collisions, which tends to reduce the translational velocity, is larger than that of inter-particle collisions. The frequency of wall-particle collisions per unit area is proportional (nu_y/L), whereas the number of inter-particle collisions is proportional to $n^2 d(u_x^2 + u_y^2)^{1/2}$. The ratio of the binary collision frequency and the particle–wall collision frequency is given by $(ndL(u_x^2 + u_y^2)^{1/2}/u_y)$. Since we are considering the limit $(ndL) = \varepsilon \ll 1$, the ratio of binary and particle–wall collisions is always small if u_x decreases to zero faster than u_y as the particle undergoes wall collisions, so that the ratio $((u_x^2 + u_y^2)^{1/2}/u_y)$ is close to 1. Therefore, it is expected that the final steady state will be one in which the translational velocities of the particles reduce to zero if u_x reduces to zero faster than u_y as the particle undergoes wall collisions.
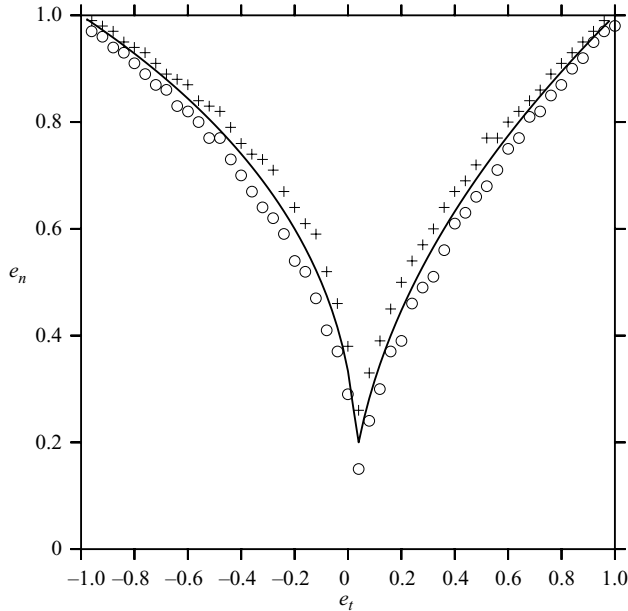
V. Kumaran

FIGURE 2. Static and dynamic regions for different values of e_t and e_n, and $\kappa = 0.5$: +, parameter values corresponding to static steady state from simulations for $\varepsilon = 0.0001$; $\bigcirc$, parameter values corresponding to dynamic steady state from simulations for $\varepsilon = 0.0001$; —, theoretical prediction for the boundary between static and dynamic steady states.

In the opposite case, where u_y reduces to zero faster than u_x as the particle collides with the wall, it is expected that $((u_x^2 + u_y^2)/u_y)$ will increase with the number of collisions, and this ratio could be large enough that $(ndL(u_x^2 + u_y^2)^{1/2}/u_y)$ will be $O(1)$ even though ndL is small. For example, consider $u_x \propto \lambda_{x\Omega}^i$ and $u_y \propto \lambda_y^i$, where i is the number of pairs of wall collisions since the most recent binary collision. For $\lambda_{x\Omega} < \lambda_y$, the streamwise velocity decreases to zero faster than the cross-stream velocity, and the final state is a static state consisting of particles with zero linear velocity and angular velocity equal to $(-2V_w/d)$. For $\lambda_y < \lambda_{x\Omega}$ the cross-stream velocity decreases to zero faster than the streamwise velocity, and the frequencies of binary and wall collisions are of equal magnitude when the number of pairs of wall collisions is $i = i_m \sim (\log(ndL)/\log(\lambda_y/\lambda_{x\Omega}))$. At this point, there is a high probability of a particle undergoing a binary collision, and thereby regenerating the velocity fluctuations which result in further wall collisions. Thus, the translational velocities of the particles do not reduce to zero at long time, but attain some final distribution with a non-zero standard deviation.

The results anticipated from the above analysis are in good agreement with the results of simulations. Figure 2 shows the boundary between the parameter regimes for the zero translational energy steady state, and the non-zero translational energy steady state. The points are the parameter values for which simulations were carried out on either side of the boundary: the plusses are the points at which the final steady state had zero translational energy, and the circles are the points at which the final steady state had non-zero energy. It is found that there is good agreement between theory and simulations. The distinction between final steady states with zero and non-zero translational energy is shown in figure 3. This plots the variation of $\langle u_x^2 \rangle$ and $\langle u_y^2 \rangle$, the mean-square velocities in the streamwise and cross-stream direction, as
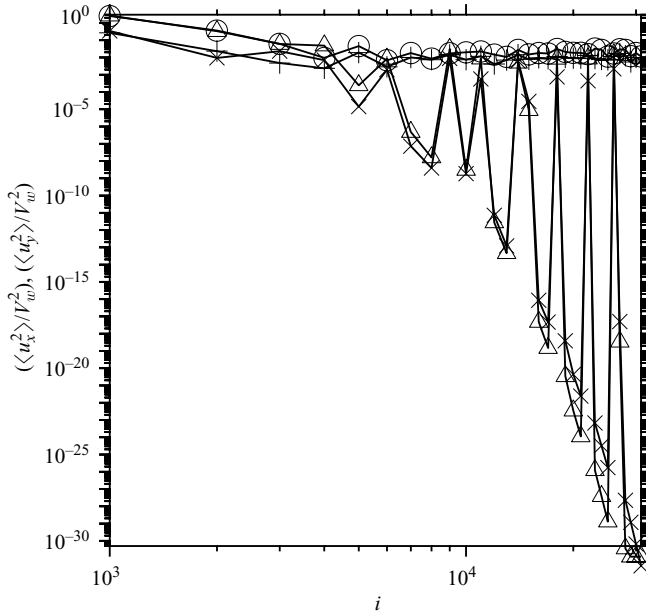
FIGURE 3. Variation of streamwise and cross-stream mean-square velocities as a function of the number of wall collisions at $e_t = 0.84$ and $\varepsilon = 0.0001$. $\triangle$, $(\langle u_x^2 \rangle / V_w^2)$; $\times$, $(\langle u_y^2 \rangle / V_w^2)$ for $e_n = 0.92$ corresponding to the static steady state, and $\bigcirc$, $(\langle u_x^2 \rangle / V_w^2)$; $+$, $(\langle u_y^2 \rangle / V_w^2)$ for $e_n = 0.91$ corresponding to the dynamic steady state.

a function of number of collisions with the wall. It is observed that when the final steady state has zero translational energy, there is a steady decrease in the energy due to wall collisions, and periodic increases in the energy for every inter-particle collision. However, in the long term, the decrease in the energy due to wall collisions is faster than the increase due to inter-particle collisions, and the system reaches a final state where the energy decreases below machine precision. However, when the final state has non-zero translational energy, the translational energy approaches a steady value as the number of collisions increases. Next, we examine the velocity distribution and its moments in the 'dynamic' steady state with non-zero translational energy.

2.4. *Distribution function for the dynamic steady state*

At steady state, the number of particles in a differential volume in velocity space is determined by a balance between the number of particles entering and leaving that differential volume due to particle–particle and particle–wall collisions. The frequency of particle–wall collisions per unit length of the top and bottom plates is proportional to nu_y and the frequency of inter-particle collisions is proportional to $n^2 du_x L$ for $u_x \gg u_y$. These two frequencies are of equal magnitude for $(u_y/u_x) \sim \varepsilon$, where $\varepsilon = (ndL) \ll 1$.

The velocity distribution function can be inferred by following the evolution of the velocity of a particle after a binary collision. If $u_x^{(0)}$, $u_y^{(0)}$ and $\omega^{(0)}$ are the components of the velocity of a particle after a binary collision, and the average particle undergoes i_m wall collisions between two inter-particle collisions, the magnitudes of the velocity after i_m subsequent wall collisions are $(\lambda_{x\Omega}^{i_m} u_x^{(0)}, \lambda_y^{i_m} u_y^{(0)}, (\lambda_{x\Omega}^{i_m}(\omega^{(0)} + 2V_w/d) - 2V_w/d)$ from equations (2.15) and (2.16). It is shown a little later, in equation (2.19), that i_m is large. Since the eigenvalues $\lambda_{x\Omega}$ and λ_y are less than 1, the translational velocity after

i_m wall collisions is small compared to those after the most recent binary collision, while the rotational velocity is close to $(-2V_w/d)$. Therefore, a typical binary collision involves two particles with translational velocities close to zero, and rotational velocity close to $(-2V_w/d)$. A collision between two such particles will result in post-collisional linear velocities of the particles proportional to V_w. The exact expression for the post-collisional velocities can be evaluated as follows. Consider a collision between two particles whose translational velocities are zero in the leading approximation, while the rotational velocities are equal to $\omega = (-2V_w/d)$. However, the relative translational velocity of the particles is along the x-axis in the leading approximation, since $u_x \gg u_y$ for the colliding particles. When these two particles collide, the final velocity after the collision depends on the angle θ between the relative velocity and the line joining the centres of the particles. Because $u_x \gg u_y$ for the colliding particles, the angle θ is also the angle between the line joining centres and the x-axis. The final velocities after the binary collision can be easily determined using the collision rules (2.7), (2.8) and (2.9) as

$$\left. \begin{array}{l} u_x^{(0)} = -2\eta_2 V_w \sin(\theta), \\ u_y^{(0)} = 2\eta_2 V_w \cos(\theta), \\ \Omega^{(0)} = (4\eta_2 V_w/d\kappa), \end{array} \right\} \tag{2.17}$$

where $\eta_2 = ((1+e_t)/2)(\kappa/(1+\kappa))$. Consequently, both $u_x^{(0)}$ and $u_y^{(0)}$ scale as V_w. Therefore, the linear and angular velocities of the particles after i pairs of particle–wall collisions scale as

$$\left. \begin{array}{l} u_x^{(i)} \sim \lambda_{x\Omega}^i V_w, \\ u_y^{(i)} \sim \lambda_y^i V_w, \\ \Omega^{(i)} \sim \lambda_{x\Omega}^i (V_w/d), \end{array} \right\} \tag{2.18}$$

where $\Omega^{(i)} = \omega^{(i)} + (2V_w/d)$.

As the particle undergoes wall collisions, the y-component of the velocity decreases faster than the x-component, since $\lambda_y < \lambda_{x\Omega}$ for the dynamic steady state. The frequency of particle–wall collisions is proportional to $nu_y^{(i)} f(u_x^{(i)}, u_y^{(i)})$, while that of binary collisions is proportional to $n^2 dL(u_x^{(i)2}+u_y^{(i)2})^{1/2} \sim n^2 dL u_x^{(i)}$. Therefore, the ratio of particle–particle collisions and particle–wall collisions is $(u_x^{(i)}\varepsilon/u_y^{(i)}) \sim (\lambda_{x\Omega}/\lambda_y)^i \varepsilon$. This ratio is of $O(1)$ for

$$i = i_m \sim (\log(\varepsilon)/\log(\lambda_y/\lambda_{x\Omega})). \tag{2.19}$$

Therefore, after i_m collisions, the frequencies of particle–particle and particle–wall collisions are of equal magnitude, and for $i \gg i_m$, the frequency of particle–particle collisions is large compared to that of particle–wall collisions. The magnitudes of the velocity components for the cross-over from the particle–wall-collision-dominated regime to the particle–particle-collision-dominated regime are

$$\left. \begin{array}{l} u_x \sim V_w \lambda_{x\Omega}^{i_m} \sim V_w \varepsilon^{(\log(\lambda_{x\Omega})/\log(\lambda_y/\lambda_{x\Omega}))}, \\ u_y \sim V_w \lambda_y^{i_m} \sim V_w \varepsilon^{(\log(\lambda_y)/\log(\lambda_y/\lambda_{x\Omega}))}, \\ \omega + (2V_w/d) \sim (V_w/d)\lambda_{x\Omega}^{i_m} \sim (V_w/d)\varepsilon^{(\log(\lambda_{x\Omega})/\log(\lambda_y/\lambda_{x\Omega}))}. \end{array} \right\} \tag{2.20}$$

The physical picture of the evolution of the particle velocity is as follows. The frequency of binary collisions is of the same magnitude as that of particle–wall collisions only for $u_x \ll V_w$ and $u_y \ll V_w$, for which $(u_x/u_y) \sim \varepsilon^{-1}$. Therefore, a binary collision scatters particles from a pre-collisional state with near-zero translational

velocity and a rotational velocity close to $-(2V_w/d)$, to a post-collisional state in which the magnitudes of both the velocity components are V_w. When the translational velocity of the particles is $O(V_w)$, the frequency of wall collisions is large compared to that of binary collisions, and so the particle undergoes repeated collisions with the walls and comes down the velocity cascade according to equations (2.15) and (2.16). This process continues until the velocity decreases to $u_x \ll V_w$, $u_y \ll V_w$ and $(u_x/u_y) \sim \varepsilon^{-1}$. The number of pairs of wall collisions required for the particle velocity to decrease to this value is $i_m = (\log(\varepsilon)/\log(\lambda_y/\lambda_{x\Omega}))$. At this level in the velocity cascade, the probability of a binary collision is equal to that of a wall collision, and a particle undergoes a binary collision for $i \sim i_m$. In this manner, a dynamical steady state is achieved.

It is convenient to define a velocity distribution $f_i(\theta)$ parameterized by the number of pairs of particle–wall collisions after the most recent particle–particle collision i, which is defined such that $n f_i(\theta)\, d\theta$ is the number of particles per unit area which have undergone i pairs of collisions after the most recent binary collision, and for which the angle between the line joining the centres and the x-coordinate at the most recent binary collision is in the differential angle $d\theta$ about θ. Note that θ is the angle between the x-axis and the line joining the centres of the particles after the most recent binary collision, for which the post-collisional velocity is given by equation (2.17). Once the post-collisional velocity after the most recent binary collision is known as a function of θ from equation (2.17), the velocity after the ith wall collision can be calculated as a function of θ and i using the recurrence relations (2.15) and (2.16). The velocity distribution function $f(u_x, u_y, \Omega)$ can be formally expressed in terms of $f_i(\theta)$ by

$$f(u_x, u_y, \Omega) = \sum_i \int d\theta\, f_i(\theta) \delta\big(u_x - u_x^{(i)}\big) \delta\big(u_y - u_y^{(i)}\big) \delta\big(\Omega - \Omega^{(i)}\big) \tag{2.21}$$

where $u_x^{(i)}$, $u_y^{(i)}$ and $\Omega^{(i)}$ are given in (2.15) and (2.16).

The distribution function $f_i(\theta)$ at steady state is determined by a balance between an accumulation and a depletion term. The accumulation for particles with i pairs of wall collisions is due to particles with $(i-1)$ pairs of wall collisions which undergo a subsequent collision with the wall. The frequency of these collisions per unit length of the channel is

$$N_{in}^{(i)}(\theta) = n \big| u_y^{(i-1)} \big| f_{i-1}(\theta). \tag{2.22}$$

Note that there is no accumulation of particles for $i > 0$ due to binary collisions, since a binary collision sets the wall collision index of the particles to zero. The accumulation of particles for $i = 0$ due to binary collisions is determined later in equations (2.32) and (2.33).

The depletion of particles with i wall collisions after the most recent binary collision could be due to a collision of the particle with the wall or with another particle. The rate of depletion of particles due to collisions with the wall per unit length of the channel is

$$N_{out}^{(i)\prime}(\theta) = n \big| u_y^{(i)} \big| f_i(\theta). \tag{2.23}$$

For $i \ll i_m$, we would expect equation (2.23) to provide the total rate of depletion of particles, since the rate of depletion due to binary collisions is small compared to that due to wall collisions. In this case, the distribution function is given by equating (2.22) and (2.23),

$$f_i = \lambda_y^{-1} f_{i-1} = \lambda_y^{-i} f_0. \tag{2.24}$$

Note that the above equation is valid only for $i \ll i_m$, and is modified by the rate of depletion of particles due to binary collisions for $i \sim i_m$. The value of the distribution function for $i \sim i_m$ can be estimated as,

$$f_i \sim \lambda_y^{-i_m} f_0 \sim f_0 \varepsilon^{(\log(\lambda_y)/\log(\lambda_y/\lambda_{x\Omega}))}. \tag{2.25}$$

Though equation (2.24) has provided an expression for the distribution function for $i \ll i_m$, we do not yet have an estimate of f_i for $i \gg i_m$. This estimate is obtained by explicitly considering the depletion of particles due to binary collisions.

The exact expression for the rate of depletion of particles due to binary collisions, assuming molecular chaos, is

$$N_{out}^{(i)''} = n^2 dL \sum_j \int d\theta' \int d\boldsymbol{k}\, f_i(\theta) f_j(\theta') \big(\boldsymbol{u}^{(i)} - \boldsymbol{u}^{(j)}\big) \cdot \boldsymbol{k} \tag{2.26}$$

where $\boldsymbol{k}$ is the unit vector in direction of the line joining the centres of the particles, and the integral over $\boldsymbol{k}$ is carried out only for particles which approach before a collision, i.e. for which $(\boldsymbol{u}^{(i)} - \boldsymbol{u}^{(j)}) \cdot \boldsymbol{k} > 0$. Note that there is a factor L in (2.26) because we consider the rate of depletion per unit width of the channel. Equation (2.26) is difficult to analyse, and so we seek a uniform approximation for this flux which is valid for both the wall-collision-dominated regime $i \ll i_m$ and the binary-collision-dominated regime $i \gg i_m$. Consider the collision of a particle in the latter regime $i \gg i_m$ with a second particle that has wall collision index j.

(*a*) If the second particle has wall collision index $j \ll i_m$, the velocity of the second particle is $u_x^{(j)} \sim V_w$, and the distribution function $f \sim f_0$. The collision rate per unit width of the channel is proportional to $n^2 dL V_w f_0$.

(*b*) If the second particle has wall collision index $j \sim i_m$, then $u_x^{(j)} \sim V_w \lambda_{x\Omega}^{i_m}$, and $f \sim \lambda_y^{(-i_m)} f_0$ from equation (2.24). The collision rate per unit width of the channel is $n^2 dL V_w (\lambda_{x\Omega}/\lambda_y)^{i_m} f_0 \sim n^2 dL V_w f_0 \varepsilon^{-1}$, since $i_m = \log(\varepsilon)/\log(\lambda_y/\lambda_{x\Omega})$.

(*c*) If $j \gg i_m$, we show below that the distribution function decreases proportionally to $\lambda_y^{j^2/2}$ while the particle velocity in the x-direction decreases proportionally to $\lambda_{x\Omega}^j$. Therefore, the collision rate per unit width of the channel is proportionally to $n^2 dL f_0 \lambda_y^{j^2} \lambda_{x\Omega}^j V_w$. For $j \gg i_m$, it can easily be verified that this collision rate is small compared to the collision rate $n^2 dL V_w f_0 \varepsilon^{-1}$ for $j \sim i_m$.

From the above, it is clear that the dominant contribution to the rate of depletion of particles is due to collisions with other particles having $j \sim i_m$. For these particles, the velocity $u_x^{(j)} \gg u_x^{(i)}$ (since $j \sim i_m$ and $i \gg i_m$), and the relative velocity between the particles can be approximated as $|u_x^{(i)} - u_x^{(j)}| = u_x^{(j)}$. Therefore, the rate of depletion due to binary collisions can be approximated as,

$$N_{out}^{(i)''} = n^2 dL f_i(\theta) \sum_j \int d\theta' |u_x^{(j)}| f_j(\theta')$$

$$= A n^2 dL f_i(\theta) V_w \lambda_{x\Omega}^{i_m}$$

$$= A n^2 dL f_i(\theta) V_w \varepsilon^{(\log(\lambda_{x\Omega})/\log(\lambda_y/\lambda_{x\Omega}))}$$

$$= A n f_i(\theta) \varepsilon^{(\log(\lambda_y)/\log(\lambda_y/\lambda_{x\Omega}))} \tag{2.27}$$

where A is a function of the coefficients of restitution, but is not a function of ε in the limit $\varepsilon \to 0$, because the ε dependence is incorporated into the last term on the

right-hand side of equation (2.27). Note that the above equation is a definition of A,

$$A = \left(\sum_j \int d\theta' |u_x^{(j)}| f_j\right) / \left(V_w \lambda_{x\Omega}^{i_m}\right). \tag{2.28}$$

It should be noted that A cannot be evaluated at the present stage, since the distribution function is not yet evaluated, but it can be evaluated self-consistently along with the distribution function after we have an expression for the distribution function in terms of A. Equation (2.27) for the flux is exact for particles with number of wall collisions $i \gg i_m$ and $u_x^{(i)} \ll u_x^{(i_m)}$. For particles with $i \ll i_m$, it is significantly in error, because $u_x^{(i)}$ and $u_y^{(i)}$ are of the same magnitude, and $u_x^{(i)}$ is not small compared to $u_x^{(j)}$. However, it should be noted that for these particles, the depletion rate due to binary collisions (2.27) is $O(\varepsilon)$ smaller than the depletion rate due to wall collisions (2.23), and therefore the sum of equations (2.23) and (2.27) provides a uniform approximation for the depletion rate for both $i \ll i_m$ and $i \gg i_m$. With this uniform approximation for the rate of depletion of particles due to binary collisions, the total rate of depletion of particles is

$$\begin{aligned} N_{out}^{(i)} &= n\left(|u_y^{(i)}| + A\varepsilon^{(\log(\lambda_y)/\log(\lambda_y/\lambda_{x\Omega}))} V_w\right) f_i \\ &= n\left(|u_y^{(0)}|\lambda_y^i + A\lambda_y^{i_m} V_w\right) f_i. \end{aligned} \tag{2.29}$$

At steady state, a balance between the rate of increase and decrease provides the recurrence relation for the distribution function,

$$\begin{aligned} f_i(\theta) &= \frac{\lambda_y^{i-1}|u_y^{(0)}| f_{i-1}(\theta)}{\lambda_y^i |u_y^{(0)}| + A\lambda_y^{i_m} V_w} \\ &= \frac{\lambda_y^{-1} f_{i-1}}{1 + \left(A\lambda_y^{i_m-i} V_w/|u_y^{(0)}|\right)} \\ &= \frac{\lambda_y^{-i} f_0}{\prod_{j=0}^i \left(1 + \left(AV_w\lambda_y^{i_m-j} V_w/|u_y^{(0)}|\right)\right)}. \end{aligned} \tag{2.30}$$

This expression is consistent with equation (2.24) for the distribution function for $i \ll i_m$, since the denominator is close to 1. For $i \gg i_m$, the above distribution function can be approximated as,

$$f_i(\theta) \sim \left(AV_w/|u_y^{(0)}|\right)^{-i} \lambda_y^{(i(i+1)/2-ii_m-i)} f_0. \tag{2.31}$$

The function $f_0(\theta)$ is determined by a balance between the accumulation of particles whose velocity is scattered by a binary collision, and the depletion of particles due to the first wall collision. The flux of particles due to a binary collision, per unit width of the channel, can be determined using the molecular chaos approximation,

$$N_{in}^{(0)}(\theta)\, d\theta = n^2 dL \sum_i \sum_j \int d\theta' \int d\theta'' \int d\mathbf{k}\, f_i(\theta') f_j(\theta'')\left(\mathbf{u}^{(i)} - \mathbf{u}^{(j)}\right) \cdot \mathbf{k} \tag{2.32}$$

where $\mathbf{k}$ is the unit vector in the direction of the line joining the centres of the particles at collision, and the integral over $\mathbf{k}$ (equation (2.32)) is evaluated for particles which approach prior to a collision, or for $(\mathbf{u}^{(i)} - \mathbf{u}^{(j)}) \cdot \mathbf{k} \geq 0$. The integral over the velocity of the colliding particles depends on the details of the velocity distribution, which is not

known at this stage. However, this can be evaluated consistent with the approximation in equation (2.27). Scaling arguments were used to show, above equation (2.27), that the dominant contribution to binary collisions is due to collisions between particles with wall collision index $i \sim i_m$. For these particles, the streamwise velocity u_x is large compared to the cross-stream velocity u_y, and $u_x \sim \lambda_{x\Omega}^{i_m} V_w$. Therefore, the rate of accumulation of particles with wall collision index $i = 0$ can be estimated as

$$
\begin{aligned}
N_{in}^{(0)} &= g_0 n^2 \mathrm{d}L |\cos(\theta)| \left(V_w \lambda_{x\Omega}^{i_m}\right) \\
&= g_0 n |\cos(\theta)| V_w \varepsilon^{(\log(\lambda_y)/\log(\lambda_y/\lambda_{x\Omega}))}
\end{aligned}
\tag{2.33}
$$

where θ is the angle between the line joining the centres of the particles at collision and the x-axis, and g_0 is a multiplicative constant defined by the normalization condition a little later. Note that the constant g_0 is not the same as the constant A defined earlier, since we had made the assumption $|u_x^{(i)}| \ll |u_x^{(j)}|$ when defining A for a binary collision between two particles i and j in equation (2.27), whereas the constant g_0 is used to model collisions between particles i and j for which $|u_x^{(i)}| \sim |u_x^{(j)}|$.

The collisional rate of depletion of particles with wall collision index 0 due to the first wall collision is

$$
\begin{aligned}
N_{out}^{(0)} &= n |u_y^{(0)}| f_0(\theta) \\
&= n (2\eta_2 V_w |\cos(\theta)|) f_0(\theta).
\end{aligned}
\tag{2.34}
$$

Equating these, we find that f_0 is independent of θ, and

$$
f_0 = (g_0/2\eta_2) \varepsilon^{(\log(\lambda_y)/\log(\lambda_y/\lambda_{x\Omega}))}.
\tag{2.35}
$$

In (2.35), the value of g_0 is determined from the normalization requirement,

$$
\sum_i \int \mathrm{d}\theta f_i = 1
\tag{2.36}
$$

where f_i is given in terms of f_0 from the relation (2.30). With this, the uniform approximation for the distribution function f_i is

$$
f_i(\theta) = \frac{\left(\lambda_y^{-i} \varepsilon^{\log(\lambda_y)/\log(\lambda_y/\lambda_{x\Omega})} \bigg/ \prod_{j=0}^{i} \left(1 + \left(A V_w \lambda_y^{i_m - j} V_w / |u_y^{(0)}|\right)\right)\right)}{\int \mathrm{d}\theta \sum_{i=0}^{\infty} \left(\lambda_y^{-i} \varepsilon^{\log(\lambda_y)/\log(\lambda_y/\lambda_{x\Omega})} \bigg/ \prod_{j=0}^{i} \left(1 + \left(A \lambda_y^{i_m - j} V_w / |u_y^{(0)}|\right)\right)\right)}.
\tag{2.37}
$$

It is clear, from equations (2.24) and (2.31), that the distribution function decreases proportionally to $\lambda_y^{-i} f_0$ for $i \ll i_m$, and shows a much faster decrease proportionally to $\lambda_y^{i^2/2} \lambda_{x\Omega}^{i_m} f_0$ for $i \gg i_m$, and has a maximum for $i \sim i_m$. It can also be shown that the number of particles per unit area with $i < i_m$ is large compared to that with $i > i_m$. The number of particles per unit area with $i < i_m$ can be estimated by summing the approximation (2.24) for the distribution function from 0 to i_m,

$$
\begin{aligned}
n \sum_{i=0}^{i_m} f_i &\sim n \sum_{i=0}^{i_m} \lambda_y^{-i} f_0 \\
&\sim n \lambda_y^{-i_m} f_0
\end{aligned}
\tag{2.38}
$$

$$
\sim n.
\tag{2.39}
$$

The number of particles with $i > i_m$ can be estimated by summing the approximation (2.31) for the distribution function from i_m to ∞,

$$n \sum_{i=i_m}^{\infty} f_i \sim n \sum_{i=i_m}^{\infty} \lambda_y^{i^2/2} \lambda_{x\Omega}^{i_m} f_0$$

$$\sim (n f_0 / \sqrt{\log(\lambda_y^{-1})})$$

$$\sim \left(n \varepsilon^{(\log(\lambda_y)/\log(\lambda_y/\lambda_{x\Omega}))} / \sqrt{\log(\lambda_y^{-1})} \right). \tag{2.40}$$

Therefore, the number of particles for $i > i_m$ is small compared to that for $i < i_m$. Similar calculations can be carried out to determine the contributions to the moments of the velocity distribution, and these calculations indicate that the contribution to the second moments of the velocity distribution from particles with $i > i_m$ is small compared to the contribution due to particles with $i < i_m$. Therefore, the dominant contribution to the moments of the velocity distribution is due to particles with $i < i_m$, for which the distribution function f_i increases proportional to λ_y^{-i}.

Next, we numerically examine some features of the distribution function obtained above. There is one constant in equation (2.37) which is determined from self-consistency, and there is the implicit assumption that this constant tends to finite values in the limit $\varepsilon \to 0$. We examine this assumption by evaluating this constant as a function of ε for fixed values of e_t and e_n. The numerical procedure for carrying out the computations is as follows. The distribution function f_i was determined from equation (2.37). The evolution of the particle velocity in a particle–wall collision is given by equations (2.15) and (2.16), while the evolution of the particle velocity in a binary collision is given by equation (2.17). The upper limit for the wall-collision index i was assumed to be $(2\log(\varepsilon)/\log(\lambda_y/\lambda_{x\Omega}))$, which is two times the expected magnitude of i_m from equation (2.19), in all the computations. The trapezoidal rule was used for integration in the θ-coordinate, where the interval from 0 to 2π was divided into 400 intervals for the integration. It was verified that doubling this number of intervals did not alter results by more than 1%. An interative procedure required to determine the constant A is determined from the requirement of self-consistency (equation (2.28)). The iterative procedure used here was the Newton–Raphson technique, and it was verified that quadratic convergence is obtained.

The results for the constant A are shown as a function of ε for different values of the coefficients of restitution in figure 4. It is observed that the A does tend to a finite value in the limit $\varepsilon \to 0$ for all values of the coefficient of restitution, as assumed in the self-consistency equation (2.28). The value of A is in the range 1 to 100 for most values of the coefficient of restitution, though it is higher for $e_t = 0.8$ and $e_n = 0.85$. This is because the ratio $(\lambda_y/\lambda_{x\Omega}) = 1.1$ is close to 1, and the rate of decrease of u_y in wall collisions is close to the rate of decrease of u_x. Therefore, this point is close to the boundary between static and dynamical steady states in figure 2. We will see, a little later, that the rate of decrease of the velocity moments with ε is also relatively high in this case, and the agreement between theory and simulation is relatively poor for $e_t = 0.8$ and $e_n = 0.85$. However, figure 4 confirms that A approaches a constant value in the limit $\varepsilon \to 0$ for all values of the coefficient of restitution, thus validating the assumptions made in equation (2.28).

The variation of the distribution function f_i, integrated over the θ-coordinate, with the wall collision index i is shown in figure 5. As expected, the distribution function first increases for $i < i_m$, and then decreases rapidly for $i > i_m$. The distribution
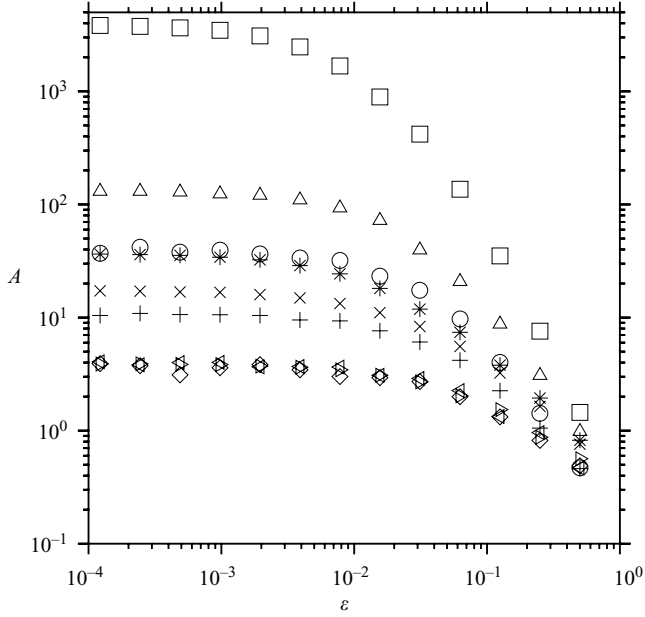
FIGURE 4. The parameter A as a function of ε determined self-consistently from equation (2.28). $\bigcirc$, $e_t = 0.6$, $e_n = 0.65$; $\triangle$, $e_t = 0.7$, $e_n = 0.75$; ∇, $e_t = 0.8$, $e_n = 0.85$; $+$, $e_t = 0.70$, $e_n = 0.70$; $\times$, $e_t = 0.80$, $e_n = 0.80$; $*$, $e_t = 0.90$, $e_n = 0.90$; $\diamond$, $e_t = 0.65$, $e_n = 0.6$; $\triangleleft$, $e_t = 0.75$, $e_n = 0.7$; $\triangleright$, $e_t = 0.85$, $e_n = 0.8$.

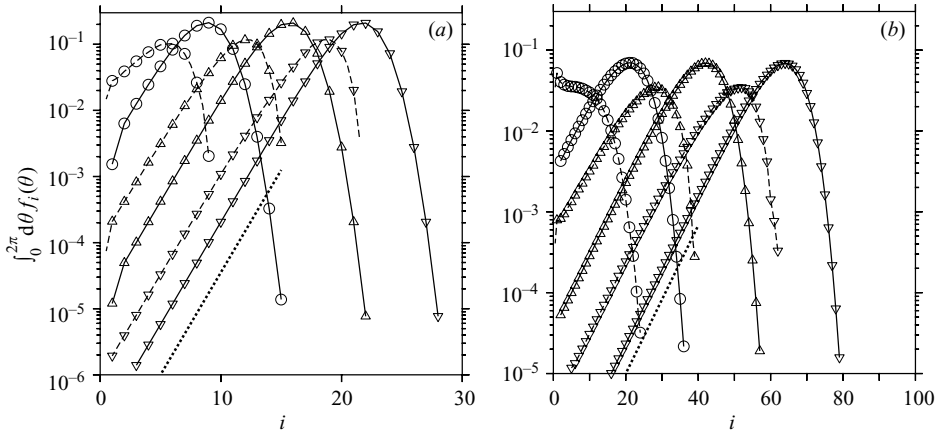FIGURE 5. The variation of $\int_0^{2\pi} \mathrm{d}\theta f_i(\theta)$ as a function of i for (a) $e_t = e_n = 0.7$ and (b) $e_t = e_n = 0.9$ $\bigcirc$, $\varepsilon = 0.01$; $\triangle$, $\varepsilon = 0.001$; ∇, $\varepsilon = 0.0001$. The solid lines show the theoretical predictions, and the dashed lines show the simulation results. The dotted lines in (a) and (b) show the theoretically predicted slopes of 0.49 and 0.81 respectively.

function f_i as a function of i was also evaluated using event-driven simulations. In these simulations, each particle was assigned a wall collision index, which was incremented by 1 for every pair of wall collisions, and which was set equal to zero at every binary collision. The distribution function f_i as a function of i was determined by averaging over all particles as described §2.1. The results of the event-driven
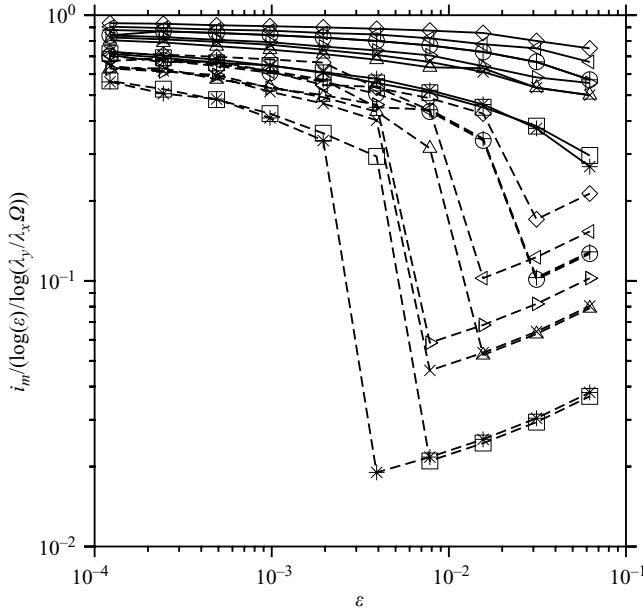
FIGURE 6. The ratio $(i_m/(\log(\varepsilon)/\log(\lambda_y/\lambda_{x\Omega})))$ as a function of ε. $\bigcirc$, $e_t = 0.6$, $e_n = 0.65$; $\triangle$, $e_t = 0.7$, $e_n = 0.75$; ∇, $e_t = 0.8$, $e_n = 0.85$; $+$, $e_t = 0.70$, $e_n = 0.70$; $\times$, $e_t = 0.80$, $e_n = 0.80$; $*$, $e_t = 0.90$, $e_n = 0.90$; $\diamond$, $e_t = 0.65$, $e_n = 0.6$; $\triangleleft$, $e_t = 0.75$, $e_n = 0.7$; $\triangleright$, $e_t = 0.85$, $e_n = 0.8$. The solid lines show the theoretical predictions and the broken lines show the simulation results.

simulations are also shown in figure 5. It is observed that the qualitative features of the distribution function obtained from simulations are in agreement with theoretical results for $\varepsilon = 0.001$ and $\varepsilon = 0.0001$, though there is some disagreement for $\varepsilon = 0.01$. The slopes of the distribution function for $i < i_m$ are in very good agreement with the theoretical predictions, and the sharp decrease of f_i for $i > i_m$ is also confirmed by simulations. However, there is a difference in the location of the maximum, with the theoretical prediction of i_m being consistently higher than the simulation result in all cases. In the case of $e_t = 0.9$ and $e_n = 0.9$, there is no clear maximum in the simulation result for $\varepsilon = 0.01$, though there is a maximum and a region of power-law increase with slope 0.81 for $\varepsilon = 0.001$ and $\varepsilon = 0.0001$, as expected from the theory.

The value i_m at which f_i is a maximum, divided by the scaling expected from equation (2.19) $(\log(\varepsilon)/\log(\lambda_y/\lambda_{x\Omega}))$, is shown for different values of ε and the coefficients of restitution in figure 6. It is observed that the ratio is close to 1, and is independent of ε in the limit $\varepsilon \to 0$, thus confirming earlier assumptions regarding the position of the peak in f_i. The value of i_m obtained from simulations is also shown in figure 6, and it is observed that the simulation result also approaches a constant value in the limit $\varepsilon \to 0$, in agreement with the theoretical prediction. However, the simulation results are consistently lower than the experimental predictions in all cases. In some cases, such as $e_t = 0.9$ and $e_n = 0.9$, the simulation result is lower than the theoretical prediction by an order of magnitude for $\varepsilon = 0.01$, but increases to about 0.5 for $\varepsilon < 0.001$. This is because, as noted in the discussion of figure 5, there is no clear maximum in the f_i vs. i graph for $e_t = 0.9$, $e_n = 0.9$ and $\varepsilon = 0.01$, though there is a clear maximum and a well-defined power-law scaling for $i < i_m$ for lower values of ε.

The theoretical prediction of i_m is consistently higher than the simulation result for the following reason. The maximum of the distribution function is the value at which the frequency of binary collisions is of the same magnitude as wall collisions. Whereas an exact expression was used for the wall collisions, an approximate expression given by (2.27) and (2.28), was used for the frequency of binary collisions. This expression is exact in the limits $i \ll i_m$, but it under-estimates the frequency of binary collisions for $i \sim i_m$. Thus, the theory over-estimates the value of i at which the frequency of particle–wall and particle–particle collisions are of equal magnitude, and this results in an over-estimation of i_m.

The moments of the velocity distribution can now be determined as

$$
\left.\begin{aligned}
\langle u_x^2 \rangle &= \int \mathrm{d}\theta \sum_{i=0}^{i_m} \left(u_x^{(i)}\right)^2 f_i(\theta), \\
\langle u_y^2 \rangle &= \int \mathrm{d}\theta \sum_{i=0}^{i_m} \left(u_y^{(i)}\right)^2 f_i(\theta), \\
\langle u_x u_y \rangle &= \int \mathrm{d}\theta \sum_{i=0}^{i_m} u_x^{(i)} u_y^{(i)} f_i(\theta).
\end{aligned}\right\}
\tag{2.41}
$$

The scaling of the moments of the distributions with ε can be evaluated analytically. For example, in the expression for u_y^2, the distribution function f_i is proportional to $\lambda_y^{-i} \varepsilon^{(\log(\lambda_y)/\log(\lambda_y/\lambda_{x\Omega}))}$ and $u_y^{(i)}$ is proportional to λ_y^i, and therefore

$$
\begin{aligned}
\langle u_y^2 \rangle &\sim \varepsilon^{(\log(\lambda_y)/\log(\lambda_y/\lambda_{x\Omega}))} \sum_{i=0}^{i_m} \lambda_y^{2i} \lambda_y^{-i} \\
&\sim \varepsilon^{(\log(\lambda_y)/\log(\lambda_y/\lambda_{x\Omega}))} \left(\frac{1 - \lambda_y^{i_m}}{1 - \lambda_y} \right) \\
&\sim \varepsilon^{(\log(\lambda_y)/\log(\lambda_y/\lambda_{x\Omega}))}.
\end{aligned}
\tag{2.42}
$$

In the last step, we have used the fact that $(\log(\lambda_y)/\log(\lambda_y/\lambda_{x\Omega}))$ is always positive for $\lambda_y < \lambda_{x\Omega}$. A similar result is obtained for the cross-correlation $\langle u_x u_y \rangle$,

$$
\langle u_x u_y \rangle \sim \varepsilon^{(\log(\lambda_y)/\log(\lambda_y/\lambda_{x\Omega}))}.
\tag{2.43}
$$

However, when a similar calculation is carried out for the moment $\langle u_x^2 \rangle$, we find that

$$
\begin{aligned}
\langle u_x^2 \rangle &\sim \varepsilon^{(\log(\lambda_y)/\log(\lambda_y/\lambda_{x\Omega}))} \sum_{i=0}^{i_m} \lambda_{x\Omega}^{2i} \lambda_y^{-i} \\
&\sim \varepsilon^{(\log(\lambda_y)/\log(\lambda_y/\lambda_{x\Omega}))} \left(\frac{1 - (\lambda_{x\Omega}^2/\lambda_y)^{(\log(\varepsilon)/\log(\lambda_y/\lambda_{x\Omega}))}}{1 - (\lambda_{x\Omega}^2/\lambda_y)} \right).
\end{aligned}
\tag{2.44}
$$

The above summation provides different scalings depending on whether $(\lambda_{x\Omega}^2/\lambda_y)$ is greater than, equal to or less than 1, as follows:

$$
\begin{aligned}
\langle u_x^2 \rangle &\sim \varepsilon^{(\log(\lambda_y)/\log(\lambda_y/\lambda_{x\Omega}))} \quad \text{for } (\lambda_{x\Omega}^2/\lambda_y) < 1 \\
&\sim \varepsilon^{(2\log(\lambda_{x\Omega})/\log(\lambda_y/\lambda_{x\Omega}))} \text{ for } (\lambda_{x\Omega}^2/\lambda_y) > 1 \\
&\sim \varepsilon^2 \frac{\log(\varepsilon)}{\log(\lambda_y/\lambda_{x\Omega})} \quad \text{for } (\lambda_{x\Omega}^2/\lambda_y) = 1.
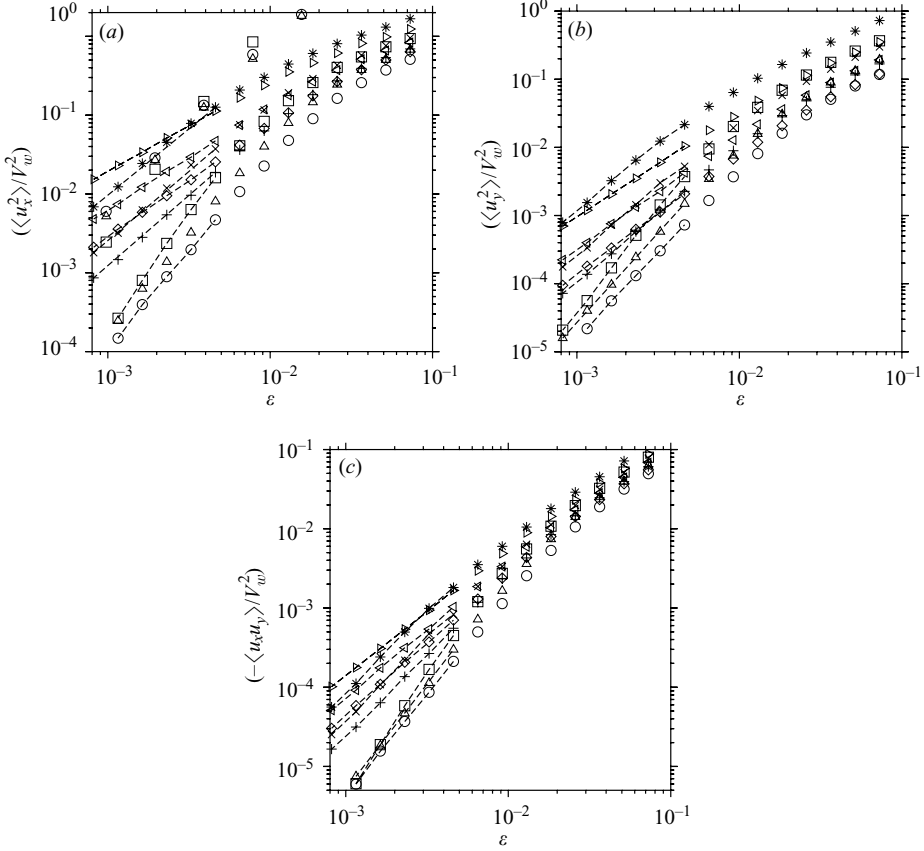\end{aligned}
\tag{2.45}
$$

FIGURE 7. The scaled second moments (*a*) $(\langle u_x^2 \rangle / V_w^2)$ (*b*) $(\langle u_y^2 \rangle / V_w^2)$ and (*c*) $(-\langle u_x u_y \rangle / V_w^2)$ as a function of ε. The slopes obtained by connecting the last five points by the dashed lines are used for purposes of comparison in table 1. $\bigcirc$, $e_t = 0.6$, $e_n = 0.65$; $\triangle$, $e_t = 0.7$, $e_n = 0.75$; ∇, $e_t = 0.8$, $e_n = 0.85$; $+$, $e_t = 0.70$, $e_n = 0.70$; $\times$, $e_t = 0.80$, $e_n = 0.80$; $*$, $e_t = 0.90$, $e_n = 0.90$; $\diamond$, $e_t = 0.65$, $e_n = 0.60$; $\triangleleft$, $e_t = 0.75$, $e_n = 0.70$; $\triangleright$, $e_t = 0.85$, $e_n = 0.80$.

Thus, the scaling of the mean-square velocity in the flow direction is sensitive to the values of the coefficients of restitution.

The variation of moments of the distribution with ε are shown in figure 7(*a*–*c*). The scalings in the limit of small ε obtained from the simulations are compared with the theoretical predictions of equations (2.42), (2.43) and (2.44) in table 1. It is observed that there is excellent agreement between the theoretical predictions and simulation results in most cases. One exception is the results for $\langle u_x^2 \rangle$ for $e_t = e_n$ (or $\lambda_{x\Omega} = \lambda_y^2$). In this case, the theoretical prediction (2.42) has a logarithmic correction ($\langle u_x^2 \rangle \sim \varepsilon^2 \log(\varepsilon)$) which is not incorporated when determining the scaling from the simulation, resulting in relatively poor agreement. The other exception is the result for $e_t = 0.80$ and $e_n = 0.85$, where the theoretically predicted slope is large, and the range of ε studied in the simulations is not sufficient to obtain convergence to the theoretically predicted scaling law.

A numerical comparison of the moments of the velocity distribution with the distribution function (2.37) indicated that the theory under-predicts the moments of the velocity distribution. The reason for this is as follows. The approximation

e_t	e_n	$\log(\langle u_x^2 \rangle)/\log(\varepsilon)$		$\log(\langle u_y^2 \rangle)/\log(\varepsilon)$		$\log(-\langle u_x u_y \rangle)/\log(\varepsilon)$	
		Theoretical	Simulation	Theoretical	Simulation	Theoretical	Simulation
0.60	0.65	2.5074	2.4865	2.5074	2.5261	2.5074	2.5696
0.70	0.75	2.6310	2.5944	2.6310	2.6285	2.6310	2.6583
0.80	0.85	3.1899	2.9858	3.1899	3.0050	3.1899	3.0736
0.70	0.70	2.0000*	1.7839	2.0000	1.9956	2.0000	2.0338
0.80	0.80	2.0000*	1.7559	2.0000	1.9869	2.0000	2.0245
0.90	0.90	2.0000*	1.6834	2.0000	1.9739	2.0000	2.0126
0.65	0.60	1.4581	1.4437	1.7291	1.7306	1.7291	1.7204
0.75	0.70	1.3516	1.3218	1.6758	1.7050	1.6758	1.6913
0.85	0.80	1.1453	1.1550	1.5727	1.5653	1.5727	1.5807

TABLE 1. The variation of $\log(\langle u_x^2 \rangle)/\log(\varepsilon)$, $\log(\langle u_y^2 \rangle)/\log(\varepsilon)$ and $\log(-\langle u_x u_y \rangle)/\log(\varepsilon)$ with the coefficients of restitution in the limit $\varepsilon \to 0$ from theory and simulations. $^*\langle u_x^2 \rangle \sim \varepsilon^2 \log(\varepsilon)$.

(2.28) clearly under-estimates the frequency of binary collisions for $|u_x^{(i)}| \sim |u_x^{(j)}|$, since there is the implicit assumption in equation (2.28) that $|u_x^{(i)}| \ll |u_x^{(j)}|$. This results in an under-estimation of the velocity moments. It is of importance to examine the sensitivity of the numerical results of the velocity moments to the binary collision frequency. For this purpose, we introduce a factor B in the term corresponding to the frequency of binary collisions in equation (2.37) as follows:

$$f_i(\theta) = \frac{\left(\lambda_y^{-i} \varepsilon^{\log(\lambda_y)/\log(\lambda_y/\lambda_x\Omega)} \Big/ \prod_{j=1}^{i} \left(1 + \left(AB\lambda_y^{i_m-j} V_w/|u_y^{(0)}|\right)\right) \right)}{\int d\theta \sum_{i=0}^{\infty} \left(\lambda_y^{-i} \varepsilon^{\log(\lambda_y)/\log(\lambda_y/\lambda_x\Omega)} \Big/ \prod_{j=1}^{i} \left(1 + \left(AB\lambda_y^{i_m-j} V_w/|u_y^{(0)}|\right)\right) \right)} \tag{2.46}$$

where the parameter A is given by the self-consistency requirement (2.28), and the parameter B is a fitted parameter to compensate for the underestimation of the binary collision frequency. We examine, numerically, the effect of this parameter B on the velocity moments in figure 8(a–c). It is expected that the numerical values of the velocity moments increase as B is increased, and it is of interest to examine whether the simulation results for the velocity moments can be reproduced using equation (2.46) with a value of B which is not much larger than 1. The approximation in equation (2.46) is valid only if the numerical value of B is not much larger than 1, and the numerical range of B required to reproduce the simulation results would be indicative of the extent of underestimation of the frequency of binary collisions in equation (2.37).

The results of the comparison are shown in figure 8(a–c). It is more convenient to plot the ratio $(\langle u_i u_j \rangle_{th}/\langle u_i u_j \rangle_{sim})$, where $\langle u_i u_j \rangle_{th}$ is the theoretically predicted value in the limit $\varepsilon \to 0$, and $\langle u_i u_j \rangle_{sim}$ is the value obtained from simulations. It is observed that the value of B required to obtain agreement between theory and simulations is a function of the coefficients of restitution, and is also different for different moments of the velocity distribution. The ratio $(\langle u_x^2 \rangle_{th}/\langle u_x^2 \rangle_{sim}) = 1$ for B between 1 and 1.5 for the range of coefficients of restitution studied here, whereas the ratio $(\langle u_y^2 \rangle_{th}/\langle u_y^2 \rangle_{sim}) = 1$ for B in the range 1–3, and $(\langle u_x u_y \rangle_{th}/\langle u_x u_y \rangle_{sim}) = 1$ for B in the range 1–2. In addition, the velocity moments are also sensitive to the value of B, and in some cases they increase by an order of magnitude for a unit increase in B. This confirms that the
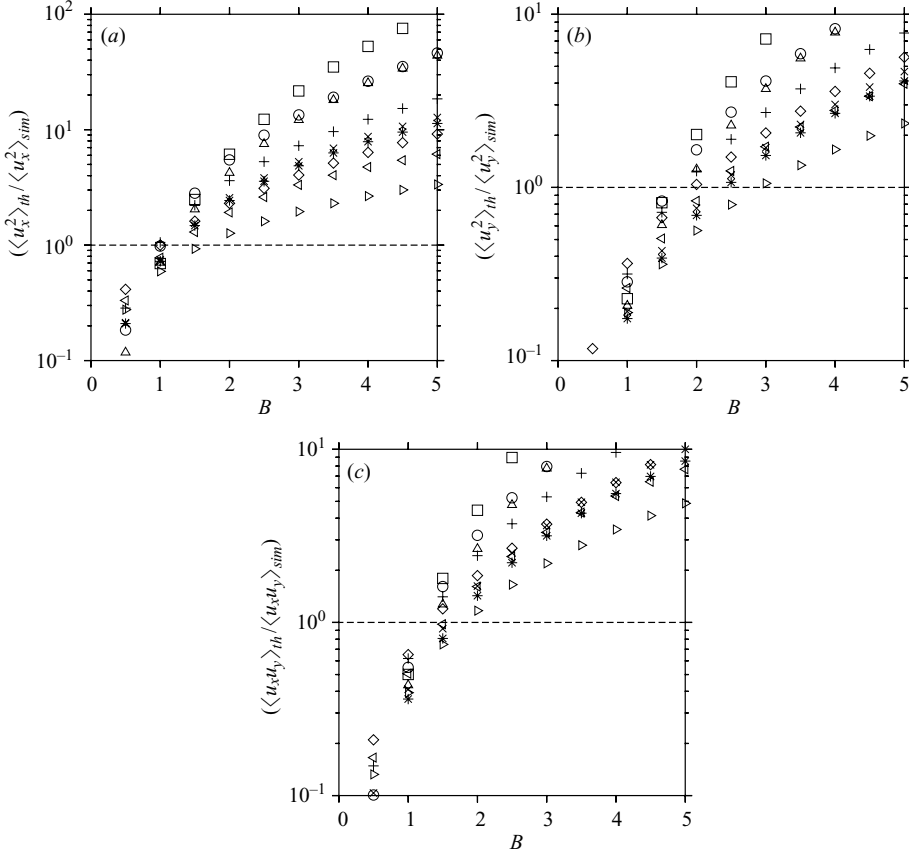
FIGURE 8. The ratio (*a*) $(\langle u_x^2 \rangle_{th}/\langle u_x^2 \rangle_{sim})$ (*b*) $(\langle u_y^2 \rangle_{th}/\langle u_y^2 \rangle_{sim})$ and (*c*) $(\langle u_x u_y \rangle_{th}/\langle u_x u_y \rangle_{sim})$ in the limit $\varepsilon \to 0$ as a function of the parameter B in equation 2.46. ○, $e_t = 0.6$, $e_n = 0.65$; △, $e_t = 0.7$, $e_n = 0.75$; ▽, $e_t = 0.8$, $e_n = 0.85$; (+), $e_t = 0.70$, $e_n = 0.70$; ×, $e_t = 0.80$, $e_n = 0.80$; *, $e_t = 0.90$, $e_n = 0.90$; ⋄, $e_t = 0.65$, $e_n = 0.60$; ◁, $e_t = 0.75$, $e_n = 0.70$; ▷, $e_t = 0.85$, $e_n = 0.80$.

frequency of binary collision is being under-estimated due to the approximation made in (2.28), though the scaling of the velocity moments with ε is correctly reproduced by the theoretical analysis.

The components of the shear stress can be determined from the velocity moments. The stress σ_{ij} is defined as the rate of transport of momentum in the i-direction across a surface whose outward unit normal is in the j-direction. The stress at a surface consists of two components: the kinetic component, due to the physical motion of particles across the surface, and the collisional component due to a collision between two particles whose centres are on either side of the surface. In the present case, the rate of transport of particles across a surface per unit length (in two dimensions) is given by nu, where n is the number density and u is the root mean square of the particle velocity. The number of collisions between two particles on either side of the surface can be estimated as follows. For two particles to collide, it is necessary for the first particle to be in a region of width d on either side of the surface, and the number of particles per unit length in a region of width d on either side of the interface to be nd. The frequency of collisions of a second particle with the first particle is ndu, where u is the root-mean-square velocity. Therefore, the number of collisions per unit width

of the surface between particles whose centres are on either side of the surface is $n^2 d^2 u$. The ratio of the number of collisions and the number of particles transported across the surface is $nd^2 = (ndL)(d/L) \ll 1$, because $(ndL) = \varepsilon \ll 1$, and the particle diameter is smaller than the channel width. Therefore, the transport of momentum is due to the kinetic mechanism in the leading approximation, and the collisional mechanism can be neglected when evaluating the transport across any surface within the channel.

It should be noted that the transport of momentum to the walls is purely collisional, since particles do not go through the walls. However, it can easily be inferred that the rate of transport of momentum across any surface within the channel is equal to the rate of transport to the walls. This is because there are no body forces in the present system, and the flow is unidirectional, and so the divergence of the stress is equal to zero. Consequently, the stress is independent of position, and the rate of transport of momentum across any surface within the flow is equal to the rate of transport of momentum to the walls. Since the rate of transport of momentum within the channel occurs predominantly by the kinetic mechanism, the stress tensor is given by (Chapman & Cowling 1970)

$$\sigma_{ij} = -n\langle u_i u_j \rangle, \tag{2.47}$$

where we have set the particle mass equal to 1, so that all masses are non-dimensionalized by the particle mass. It is apparent that the stress is equal to the number density of particles times the second moment of the velocity distribution, and so the scaling of the stress with the parameter ε is also given by equations (2.42), (2.43) and (2.45).

This section concludes with remarks regarding three surprising features of the distribution function.

(a) The above analysis has indicated that the scaling of f_i with i, as well as the scaling of the velocity moments with ε, depend on the coefficients of restitution of particle–wall collisions, but not on the coefficients of restitution of particle–particle collisions. This is because a change in the coefficient of restitution of the particle–particle collisions results in a variation of $O(1)$ in the post-collisional velocities in equation (2.17), and a variation of the coefficient of restitution in particle–wall collisions results in a change in the value of λ_y in equation (2.24) for the distribution function for $i < i_m$. However, since the frequency of particle–wall collisions is $O(i_m)$ larger than that of particle–particle collisions, a decrease in the value of λ_y would result in a decrease of $O(\lambda_y^{i_m})$ in the distribution function for $i \sim i_m$ corresponding to the maximum of the distribution function. Since $\lambda_y^{i_m} \sim \varepsilon^{(\log(\lambda_y)/\log(\lambda_y/\lambda_{x\Omega}))}$, this factor could be small compared to 1 in the limit $\varepsilon \to 0$. This is in contrast to the variation of $O(1)$ due to a variation in the coefficient of particle–particle collisions. Consequently, a variation in the coefficient of restitution of particle–particle collisions does not alter the scaling laws for the velocity distribution function or its moments.

(b) It should also be noted that the distribution function is not a function of y because we are in the high-Knudsen-number regime. In this case, the frequency of particle–wall collisions is large compared to that of particle–particle collisions, and so a particle collides with the wall many times between successive inter-particle collisions. The 'persistence length', which is the length over which the perturbation to a particle velocity persists, is equal to the distance between the walls. The particle velocity is unchanged when it travels between the two walls in the leading approximation, and so the probability of finding a particle with a given velocity is independent of y. Since the number density of the particles is independent of position, the probability of a

binary collision is also independent of position (apart from regions of thickness $(d/2)$ from the walls, where the shadow effect of the walls affects the frequency of binary collisions). Therefore, the collisional rates of accumulation and depletion of particles are also independent of position in the y-coordinate in this limit.

When the Knudsen number becomes lower, and the particle collides multiple times with other particles between two wall collisions, the persistence length for the particle velocity becomes much smaller than the channel width, and there is a variation of the density and velocity distribution in the y-direction. The same variation is not present in the high-Knudsen-number regime where a particle collides multiple times with the wall between two successive inter-particle collisions.

(*c*) The distribution function has apparently been obtained without solving the conventional Boltzmann kinetic equation for the distribution function. However, the present procedure did involve solving the Boltzmann equation for the distribution function. The unsteady term in the Boltzmann equation is neglected because we are interested in the steady distribution, while the streaming terms in the Boltzmann equation are identically zero because there are no gradients in real space, and there are no body forces on the particles. Consequently, the Boltzmann equation just reduces to setting the collision integral to zero. This is equivalent to $N_{in}^{(i)}(\theta)$ (equation (2.22)) and $N_{out}^{(i)}(\theta)$ (equation (2.29)) for $i > 0$, which leads to the solution (2.30) for the distribution function. The distribution f_0 is obtained by equating the fluxes $N_{in}^{(0)}$ (equation (2.33)) and $N_{out}^{(0)}$ (equation (2.34)).

2.5. *Three-dimensional channel*

The extension to a three-dimensional system of the analysis in §§ 2.2, 2.3 and 2.4 is briefly summarized here. In this case, the small parameter $\varepsilon = nd^2L$, where n is the number of particles per unit area. We use a coordinate system where x and y are in the flow and gradient directions respectively, and z is the vorticity direction perpendicular to the plane of flow. It is necessary to determine the evolution of three components of the linear velocity and three components of the angular velocity with particle–wall and particle–particle collisions. In the absence of particle–particle collisions, the velocities of the particles tend to a final state where the translational velocity reduces to zero, and the angular velocity in the z-direction (perpendicular to the direction of the flow) tends to $(-2V_w/d)$, while the linear velocities in the x- and y-directions tend to zero. Since the angular velocity in the cross-stream y-direction is not altered in a wall collision, this component of the angular velocity reaches a final steady-state value only due to inter-particle collisions. Therefore, in the final state, the linear velocities are all equal to zero, $u_x = u_y = u_z = 0$, the angular velocity in the x-direction is $\omega_x = 0$, the angular velocity in the z-direction is given by $\omega_z = (-2V_w/d)$, while the angular velocity in the y-direction is $\omega_y \sim O(V_w/d)$. The evolution of the particle velocities, after i pairs of wall-particle collisions, equivalent to equations (2.15) and (2.16), is

$$u_y^{(i)} = \lambda_y u_y^{(i-1)} = \lambda_y^i u_y^{(0)}, \tag{2.48}$$

$$\begin{pmatrix} u_x^{(i)} \\ \omega_z^{(i)} + 2V_w/d \end{pmatrix} = \mathbf{M} \begin{pmatrix} u_x^{(i-1)} \\ \omega_z^{(i-1)} + 2V_w/d \end{pmatrix} = \mathbf{M}^i \begin{pmatrix} u_x^{(0)} \\ \omega_z^{(0)} + 2V_w/d \end{pmatrix}, \tag{2.49}$$

$$\begin{pmatrix} u_z^{(i)} \\ \omega_x^{(i)} \end{pmatrix} = \mathbf{M} \begin{pmatrix} u_z^{(i-1)} \\ \omega_x^{(i-1)} \end{pmatrix} = \mathbf{M}^i \begin{pmatrix} u_z^{(0)} \\ \omega_x^{(0)} \end{pmatrix}, \tag{2.50}$$

It should be noted that there is a coupling in the evolution of (u_x, ω_z) and (u_z, ω_x), and the matrix **M** is the same in equations (2.49) and (2.50). Consequently, the variation in the linear and angular velocities with the number of collisions, which is the equivalent of (2.18), is

$$
\left.
\begin{aligned}
u_x^{(i)} &\sim \lambda_{x\Omega}^i V_w, \quad u_y^{(i)} \sim \lambda_y^i V_w, \quad u_z^{(i)} \sim \lambda_{x\Omega}^i V_w, \\
\omega_z^{(i)} &+ (2V_w/d) \sim \lambda_{x\Omega}^i (V_w/d), \quad \omega_x^{(i)} \sim \lambda_{x\Omega}^i (V_w/d),
\end{aligned}
\right\}
\tag{2.51}
$$

When the leading effect of particle–particle collisions is incorporated, the condition for a dynamic steady state is still given by $\lambda_{x\Omega} > \lambda_y$. Therefore, the regions of static and dynamic steady states in the (e_t, e_n)-plane are identical to those for a two-dimensional flow (figure 2). In the dynamic steady state, the mean-square velocities of the particles in the streamwise and cross-stream directions are still given by (2.42), (2.43) and (2.44), while the mean-square velocity perpendicular to the plane of flow has the same scaling as that for the mean-square velocity in the gradient direction:

$$
\begin{aligned}
\langle u_z^2 \rangle &\sim \varepsilon^{(\log(\lambda_y)/\log(\lambda_y/\lambda_{x\Omega}))} & &\text{for } (\lambda_{x\Omega}^2/\lambda_y) < 1 \\
&\sim \varepsilon^{(2\log(\lambda_{x\Omega})/\log(\lambda_y/\lambda_{x\Omega}))} & &\text{for } (\lambda_{x\Omega}^2/\lambda_y) < 1 \\
&\sim \varepsilon^2 \frac{\log(\varepsilon)}{\log(\lambda_y/\lambda_{x\Omega})} & &\text{for } (\lambda_{x\Omega}^2/\lambda_y) = 1.
\end{aligned}
\tag{2.52}
$$

3. Conclusion

In the present analysis, kinetic theory techniques were applied to determine the scaling of the velocity distribution function and the velocity moments for the shear flow of rough inelastic disks between two rough surfaces in the limit where the frequency of particle–wall collisions is large compared to that of particle–particle collisions. An asymptotic expansion was used in the small parameter $\varepsilon = (ndL)$ in two dimensions and $\varepsilon = (nd^2L)$ in three dimensions, where n is the number density (particles per unit area in two dimensions and per unit volume in three dimensions), d is the particle diameter and L is the channel width. The collision laws for rough particles (Chapman & Cowling 1970; Lun 1991) were used in the present analysis. In this model, the post-collisional velocity along the line joining centres is $-e_n$ times the pre-collisional velocity, while the post-collisional velocity perpendicular to the line joining centres is $-e_t$ times the pre-collisional velocity, where e_n and e_t are the normal and tangential coefficients of restitution.

In the leading approximation, particle–particle collisions were neglected, and it was found that, in the long time limit, the particles attain a final stationary state in which the linear velocities are equal to zero and the angular velocity is equal to the ratio of the wall velocity and the particle radius. This final static state is in contrast to the model of Kumaran (1997), where the particles have a non-zero translational velocity in the final state. When the effect of collisions in the high-Knudsen-number limit was incorporated in the analysis, it was found that there are two possible final states, depending on the relative rates of decrease of the streamwise and cross-stream velocities in wall collisions. The cross-stream velocity decreases by a factor $\lambda_y = e_n^2$ in a pair of wall collisions. When the streamwise velocity decreases faster than the cross-stream velocity, the system attains a final static state where the particles come to rest in the long time limit. However, when the cross-stream velocity decreases faster than the streamwise velocity due to particle collisions with the wall, it is shown that there is a final dynamical steady state in which the mean-square

velocity of the particles is non-zero. Since the decrease in the streamwise and cross-stream velocities is related to the tangential and normal coefficients of restitution, this condition provided a prediction for the domains in the (e_t, e_n)-plane where the static and dynamic steady states are observed in the long time limit. This prediction was found to be in quantitative agreement with simulations.

The theoretical analysis also predicted that the mean-square velocities decrease as a power of the parameter ε in the limit $\varepsilon \to 0$. The mean-square velocities $\langle u_y^2 \rangle$ and $\langle u_x u_y \rangle$ decrease proportionally to $\varepsilon^{(\log(\lambda_y)/\log(\lambda_y/\lambda_{x\Omega}))}$ in the limit $\varepsilon \to 0$. The scaling of the mean-square velocity $\langle u_x^2 \rangle$ depends on the ratio $(\lambda_{x\Omega}^2/\lambda_y)$. It is found that $\langle u_x^2 \rangle \sim \varepsilon^{(\log(\lambda_y)/\log(\lambda_y/\lambda_{x\Omega}))}$ for $(\lambda_{x\Omega}^2/\lambda_y) < 1$, and is proportional to $\varepsilon^{(2\log(\lambda_{x\Omega})/\log(\lambda_y/\lambda_{x\Omega}))}$ for $(\lambda_{x\Omega}^2/\lambda_y) > 1$. Since the mean-square velocities are proportional to the components of the stress in the three directions, this implies that the anisotropy in the stress tensor is sensitive to the coefficients of restitution. The three components of the stress tensor (in two dimensions) are of equal magnitude for $(\lambda_{x\Omega}^2/\lambda_y) < 1$, but the normal stress in the flow direction is large compared to the other two components of the stress for $(\lambda_{x\Omega}^2/\lambda_y) > 1$. The power-law scaling of the stress components with the Knudsen number is different from the result of Kumaran (1997), where it was found that the normal stress in the flow direction remains a constant in the limit $\varepsilon \to 0$, the normal stress in the cross-stream direction decreases proportionally to ε, and the shear stress is proportional to $\varepsilon \log(\varepsilon)$. Thus, both the scaling of the components of the stress tensor and the anisotropy in the stress tensor are sensitive to the details of the wall-particle interactions.

The theoretical analysis involved an approximation in equation (2.28), and this approximation resulted in an under-estimation of the binary collision frequency. It was found that due to this approximation, the numerical values of the velocity moments obtained from the theory were consistently lower than the corresponding values obtained from simulations. The sensitivity of the numerical results to the frequency of binary collisions was examined, and it was found that it is possible to obtain agreement between theory and simulations if the binary collision frequency is increased. This indicates that all of the scalings obtained by the theoretical analysis are accurate, but the frequency of binary collisions is under-estimated by a factor of $O(1)$.

The implications of the analysis for the relationship between the stress and strain rate for high-Knudsen-number flows are as follows. The shear stress exerted on the top and bottom surfaces, scaled by the particle mass, is proportional to $n V_w^2 \varepsilon^{(\log(\lambda_y)/\log(\lambda_y/\lambda_{x\Omega}))}$, where V_w is the wall velocity. Consequently, the shear stress scales as the square of the wall velocity in this limit, and the 'Bagnold coefficient', which is $(\sigma_{xy}/(V_w/L)^2)$, is proportional to $(nL^2)\varepsilon^{(\log(\lambda_y)/\log(\lambda_{x\Omega}/\lambda_y))}$. The Bagnold coefficient for the normal stress in the cross-stream direction, is also proportional to $(nL^2)\varepsilon^{(\log(\lambda_y)/\log(\lambda_{x\Omega}/\lambda_y))}$. The Bagnold coefficient for the normal stress in the streamwise direction depends on the value of $(\lambda_{x\Omega}^2/\lambda_y)$, but it is proportional to (nL^2) times a power of ε. This is very different from the behaviour in the low-Knudsen-number limit, where the Bagnold coefficient is independent of the channel width L, and is proportional to $(nd^2)^{-1}$ times a function of the coefficients of restitution in the dilute limit. The effective high-Knudsen-number limiting values of the Bagnold coefficients of the smooth particle model of Kumaran (1997), and the present rough particle model, are compared with the values in the low-Knudsen-number limit in table 2. This table indicates that the Bagnold coefficient is much smaller in the high-Knudsen-number regime than it is in the low-Knudsen-number regime.

A more appropriate manner of scaling the stress in the high-Knudsen-number regime is to divide it by V_w^2, so that the scaled stress (σ_{ij}/V_w^2) is only a function of

	High Kn Smooth	High Kn Rough	Low Kn Dilute	Low Kn Dense
$(\sigma_{xx}/(V_w/L)^2)$ $(\lambda_{x\Omega}^2 < \lambda_y)$	nL^2	$nL^2\varepsilon^{(\log(\lambda_y)/\log(\lambda_y/\lambda_{x\Omega}))}$	$(nd^4)^{-1}$	d^{-1}
$(\sigma_{xx}/(V_w/L)^2)$ $(\lambda_{x\Omega}^2 > \lambda_y)$	nL^2	$nL^2\varepsilon^{(2\log(\lambda_{x\Omega})/\log(\lambda_y/\lambda_{x\Omega}))}$	$(nd^4)^{-1}$	d^{-1}
$(\sigma_{yy}/(V_w/L)^2)$	$nL^2\varepsilon$	$nL^2\varepsilon^{(\log(\lambda_y)/\log(\lambda_y/\lambda_{x\Omega}))}$	$(nd^4)^{-1}$	d^{-1}
$(\sigma_{xy}/(V_w/L)^2)$	$nL^2\varepsilon\log(\varepsilon)$	$nL^2\varepsilon^{(\log(\lambda_y)/\log(\lambda_y/\lambda_{x\Omega}))}$	$(nd^4)^{-1}$	d^{-1}
$(\sigma_{zz}/(V_w/L)^2)$ $(\lambda_{x\Omega}^2 < \lambda_y)$	$nL^2\varepsilon$	$nL^2\varepsilon^{(\log(\lambda_y)/\log(\lambda_y/\lambda_{x\Omega}))}$	$(nd^4)^{-1}$	d^{-1}
$(\sigma_{zz}/(V_w/L)^2)$ $(\lambda_{x\Omega}^2 > \lambda_y)$	$nL^2\varepsilon$	$nL^2\varepsilon^{(2\log(\lambda_{x\Omega})/\log(\lambda_y/\lambda_{x\Omega}))}$	$(nd^4)^{-1}$	d^{-1}

TABLE 2. The scaling of the Bagnold coefficients in the high-Knudsen-number limit for smooth particles (Kumaran 1997) and rough particles (present analysis) are compared with the low-Knudsen-number limiting value. Here, $\varepsilon = (ndL)$ in two dimensions and (nd^2L) in three dimensions, where n is the number density (per unit area in two dimensions and per unit volume in three dimensions), d is the particle diameter and L is the width of the channel.

the number density n and the small parameter ε. For smooth particles (Kumaran 1997), the magnitudes of the scaled stresses are $(\sigma_{xx}/V_w^2) \sim n$, $(\sigma_{yy}/V_w^2) \sim n\varepsilon$ and $(\sigma_{xy}/V_w^2) \sim n\varepsilon\log(\varepsilon)$. For rough particles, the magnitudes of the scaled stress are $(\sigma_{xy}/V_w^2) \sim (\sigma_{yy}/V_w^2) \sim n\varepsilon^{(\log(\lambda_y)/\log(\lambda_y/\lambda_{x\Omega}))}$, while the normal stress in the flow direction is $(\sigma_{xx}/V_w^2) \sim n\varepsilon^{(\log(\lambda_y)/\log(\lambda_y/\lambda_{x\Omega}))}$ for $\lambda_{x\Omega}^2 < \lambda_y$, and $(\sigma_{xx}/V_w^2) \sim n\varepsilon^{(2\log(\lambda_{x\Omega})/\log(\lambda_y/\lambda_{x\Omega}))}$ for $\lambda_{x\Omega}^2 > \lambda_y$. An issue of interest is the variation (σ_{ij}/V_w^2) as the channel width is decreased, in order to examine whether the wall velocity is a monotonic function of channel width at a constant stress, or whether there is a maximum in the velocity as the width is increased. This variation depends on whether the number density of the particles is kept a constant as the width is decreased, or whether the number of particles in the channel is kept a constant.

(a) At constant particle number density, the parameter ε decreases proportionally to the channel width L as the channel width is decreased. For the smooth particle model (Kumaran 1997), the ratio (σ_{xx}/V_w^2) remains a constant, while (σ_{xy}/V_w^2) and (σ_{yy}/V_w^2) decrease as L is decreased. In the rough particle model, in the dynamic steady state, (σ_{ij}/V_w^2) decreases as L is decreased for all components of the stress.

(b) At constant number of particles (per unit length in two dimensions and per unit area in three dimensions), the parameter ε is a constant as the width L decreased, while the number density n increases. Consequently, all components of the stress increase proportionally to L^{-1} as the channel width L is decreases.

Thus, the application of the high-Knudsen-number analysis to problems such as avalanches and chute flows would require the specification of how the number density of particles varyies as the width of the flowing layer changes in these applications.

The present analysis establishes that kinetic theory can be employed to model the relation between the stress and strain rate in the high-Knudsen-number limit for rough particles. The predictions of the kinetic theory are in quantitative agreement with the results of simulations, both for the regimes of static and dynamic steady states and for the velocity moments or stresses in the dynamic steady state. The

distribution function for rough particles is very different from a Gaussian, and shows a bimodal structure with a power-law decay at high velocity. The velocity moments scale as a power of the small parameter ε, which is the inverse of the Knudsen number in the high-Knudsen-number limit.

REFERENCES

BOSE, M. & KUMARAN, V. 2004 Velocity distribution for a two-dimensional sheared granular flow. *Phys. Rev.* E **69**, 061301–061317.

BREY, J. J., DUFTY, J. W., KIM, C.-S. & SANTOS, A. 1998 *Phys. Rev.* E **58**, 4638–4653.

CAMPBELL, C. S. & BRENNEN, C. E. 1985 Computer simulation of granular shear flows. *J. Fluid Mech.* **151**, 167–188.

CERCIGNANI, C. 1988 *The Boltzmann Equation and its Applications.* Springer.

CHAPMAN, S. & COWLING, T. G. 1970 *The Mathematical Theory of Non-uniform Gases.* Cambridge University Press.

GOLDHIRSCH, I. 2003 Rapid granular flows. *Annu. Rev. Fluid Mech.* **35**, 267–293.

JENKINS, J. T. & RICHMAN, M. W. 1985 Grad's 13-moment system for a dense gas of inelastic spheres. *Arch. Rat. Mech. Anal.* **87**, 355–377.

JENKINS, J. T. & RICHMAN, M. W. 1986 Boundary conditions for plane flows of smooth, nearly elastic, circular disks. *J. Fluid Mech.* **171**, 52–69.

JENKINS, J. T. & SAVAGE, S. B. 1983 A theory for the rapid flow of identical, smooth nearly elastic, spherical particles. *J. Fluid Mech.* **130**, 187–202.

KNUDSEN, M. 1909 Die Gesetze der Molekularstromung und der inneren Reibungsstromung der Gase durch Rohren. *Ann. Phys.* **28**, 75–130.

KUMARAN, V. 1997 Velocity distribution function for a dilute granular material in shear flow. *J. Fluid Mech.* **340**, 319–341.

KUMARAN, V. 1998 Velocity distribution for a dilute vibro-fluidised bed. *Phys. Rev.* E **51**, 4188–4202.

KUMARAN, V. 1999 Non-equilibrium stationary states of a particle in a gravitational field driven by a vibrating surface. *Phys. Rev. Lett.* **82**, 3248–3251.

KUMARAN, V. 2000 Asymptotic solution of the linearised Boltzmann equation for the shear flow of inelastic disks. *Physica* A **275**, 483–504.

KUMARAN, V. 2004 Constitutive relations and linear stability of a sheared granular material. *J. Fluid Mech.* **506**, 1–43.

LIOU, W. W. & FANG, Y. 2004 Forced Couette flow simulations using direct simulation Monte Carlo method, *Phys. Fluids* **16**, 4211–4225.

LOYALKA, S. K. & HAMOODI, S. A. 1990 Poiseuille flow of a rarefied gas in a cylindrical tube: Solution of linearized Boltzmann equation. *Phys. Fluids* A **2**, 2061–2065.

LUN, C. K. K. 1991 Kinetic theory for granular flow of dense, slightly inelastic, slightly rough spheres. *J. Fluid Mech.* **233**, 539–559.

LUN, C. K. K. 1996 Granular dynamics of inelastic spheres in Couette flow. *Phys. Fluids* **8**, 2868–2883.

LUN, C. K. K., SAVAGE, S. B., JEFFREY, D. J. & CHEPURNIY, N. 1984 Kinetic theories for granular flow: inelastic particles in Couette flow and slightly inelastic particles in a general flow field. *J. Fluid Mech.* **140**, 223–256.

PIDDUCK, F. B. 1992 Theory of a special type of rigid molecule. *Proc. R. Soc. Lond.* A **101**, 101–112.

SAVAGE, S. B. & JEFFREY, D. J. 1981 The stress tensor in a granular flow at high shear rates. *J. Fluid Mech.* **110**, 255–272.

SELA, N. & GOLDHIRSCH, I. 1998 Hydrodynamic equations for rapid flows of smooth inelastic spheres, to Burnett order. *J. Fluid Mech.* **361**, 41–74.

SELA, N., GOLDHIRSCH, I. & NOSKOWICZ, S. H. 1996 Kinetic theoretical study of a simply sheared two dimensional granular gas to Burnett order. *Phys. Fluids* **8**, 2337.

WILLIS, D. R. 1962 Comparison of kinetic theory analyses of linearized Couette flow. *Phys. Fluids* **5**, 127–135.

WILLIS, D. R. 1965 Mass flow through a circular orifice and a two-dimensional slit at high-Knudsen-numbers. *J. Fluid Mech.* **21**, 21–31.

ZHANG, Y., QIN, R. & EMERSON, D. R. 2005 Lattice Boltzmann simulation of rarefied gas flows in microchannels. *Phys. Rev.* E **71**, 047702–047704.